STATE OF THE CLIMATE IN 2025

ANTARCTICA AND THE SOUTHERN OCEAN

M. N. Raphael and K. R. Clem, Eds.

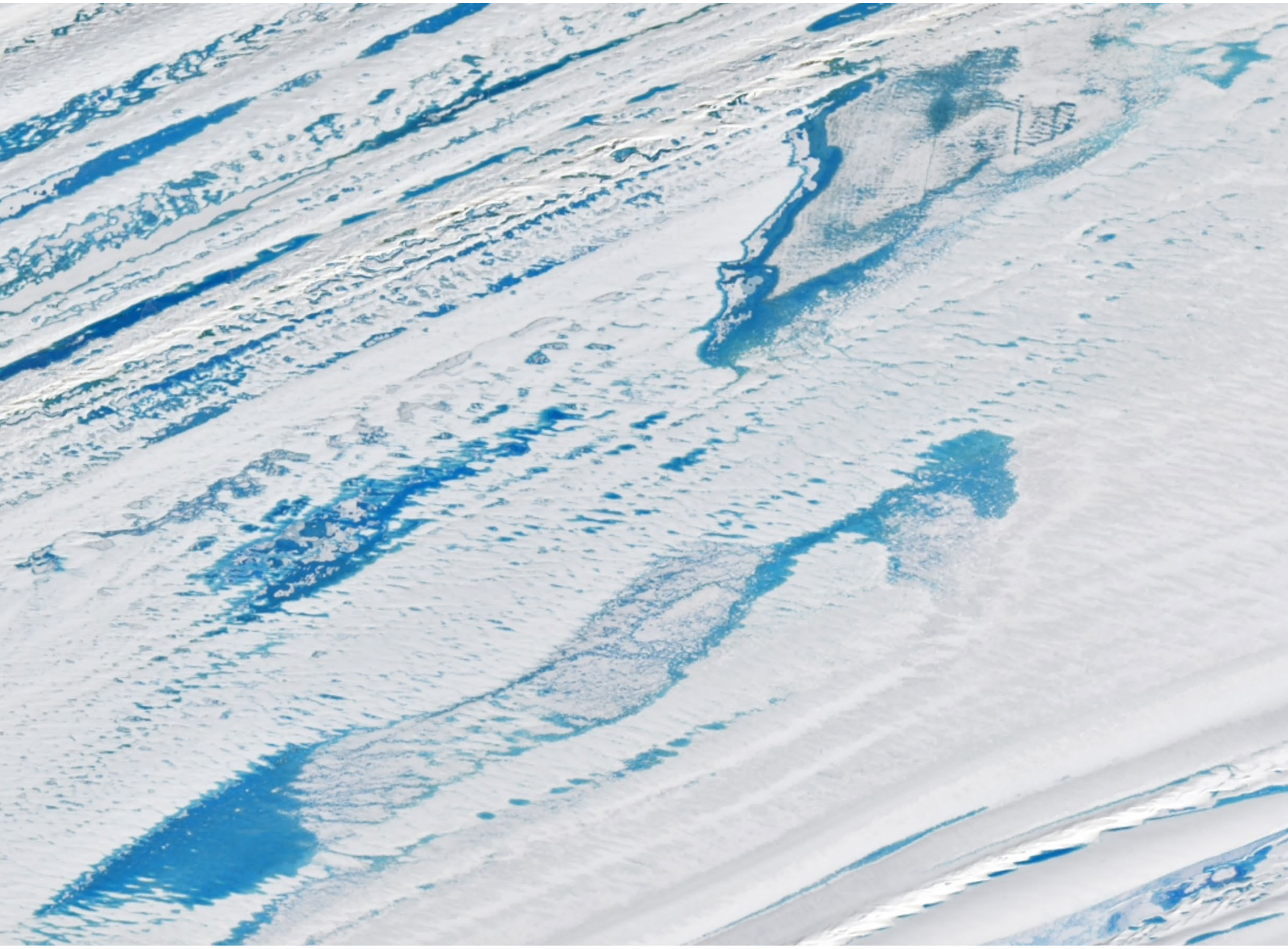

Special Online Supplement to the *Bulletin of the American Meteorological Society* Vol. 107, No. 8, August, 2026

https://doi.org/10.1175/BAMS-D-26-0127.1

Corresponding author: Marilyn N. Raphael / raphael@geog.ucla.edu

STATE OF THE CLIMATE IN 2025
Antarctica and the Southern Ocean

Editors

Jessica Blunden
James Reagan

Chapter Editors

Anthony Arguez
Josh Blannin
Peter Bissolli
Kyle R. Clem
Howard J. Diamond
Matthew L. Druckenmiller
Robert J. H. Dunn
Catherine Ganter
Nadine Gobron
Rodney Martinez
Twila A. Moon
Gary A. Morris
Marilyn N. Raphael
Renellys C. Perez
Carl J. Schreck III
Zewdu Segele
Laura Stevens
Richard L. Thoman
Denis L. Volkov
Zhiwei Zhu

Technical Editors

Lukas Noguchi
Laura Ohlmann

BAMS Special Editor for Climate

Timothy DelSole

American Meteorological Society

Cover Credit:

Meltwater ponds on the Amery ice shelf during the Antarctic melt season in late 2024. NASA Earth Observatory images by Wanmei Liang, using Landsat data from the U.S. Geological Survey.

How to cite this document:

Antarctica and the Southern Ocean is one chapter from the *State of the Climate in 2025* annual report and is available from https://doi.org/10.1175/BAMS-D-26-0127.1. Compiled by NOAA's National Centers for Environmental Information, *State of the Climate in 2025* is based on contributions from scientists from around the world. It provides a detailed update on global climate indicators, notable weather events, and other data collected by environmental monitoring stations and instruments located on land, water, ice, and in space. The full report is available from https://doi.org/10.1175/2026BAMSStateoftheClimate.1.

Citing the complete report:

Blunden, J. and J. Reagan, Eds., 2026: "State of the Climate in 2025". Bull. Amer. Meteor. Soc., 107 (8), Si–S512, https://doi.org/10.1175/2026BAMSStateoftheClimate.1.

Citing this chapter:

Raphael, M. N. and K. R. Clem, 2026: Antarctica and the Southern Ocean [in "State of the Climate in 2025"]. Bull. Amer. Meteor. Soc., 107 (8), S352–S396, https://doi.org/10.1175/BAMS-D-26-0127.1.

Citing a section (example):

Bahrami, M., E. Glen, L. D. Trusel, A. F. Banwell, P. Jackson, and R. L. Dell, 2026: The exceptional nature of supraglacial meltwater in 2024/25 [in "State of the Climate in 2025"]. Bull. Amer. Meteor. Soc., 107 (8), S372–S375, https://doi.org/10.1175/BAMS-D-26-0127.1.

Editor and Author Affiliations (alphabetical by name)

Adjou, Mohamed, ISEN Engineering School, LaBISEN, Knowledge Learning and Information Modeling (KLaIM), Brest, France; University of Brest, Institut Universitaire Européen de la Mer (IUEM) UAR3113, Plouzané, France

Adusumilli, Susheel, Department of Earth Sciences, University of Oregon, Eugene, Oregon

Amory, Charles, Université Grenoble Alpes, Institut des Géosciences de l'Environnement, IRD, CNRS, Grenoble INP, Grenoble, France

Bahrami, Mahsa, Department of Geography, Pennsylvania State University, State College, Pennsylvania

Baiman, Rebecca, Department of Atmospheric Science, Colorado State University, Fort Collins, Colorado

Banwell, Alison F., Centre for Polar Observation and Modelling, School of Geography and Natural Sciences, Northumbria University, Newcastle upon Tyne, United Kingdom; Cooperative Institute for Research in Environmental Sciences, University of Colorado Boulder, Boulder, Colorado

Barreira, Sandra, Argentine Naval Hydrographic Service, Buenos Aires, Argentina

Beadling, Rebecca L., Department of Earth and Environmental Science, Temple University, Philadelphia, Pennsylvania

Black, T., NASA Goddard Space Flight Center, Greenbelt, Maryland

Brown, Meghan, Department of Earth Sciences, University of Oregon, Eugene, Oregon

Clem, Kyle R., School of Geography, Environment and Earth Sciences, Victoria University of Wellington, Wellington, New Zealand

Colwell, Steve, British Antarctic Survey, Cambridge, United Kingdom

Coy, Lawrence, NASA Goddard Space Flight Center, Greenbelt, Maryland; Science Systems and Applications, Inc., Lanham, Maryland

Cullis, P., NOAA/OAR Earth System Research Laboratory, Global Monitoring Division, Boulder, Colorado; University of Colorado Boulder, Boulder, Colorado

Datta, Rajashree T., Department of Civil Engineering and Geosciences, TU Delft, Delft, The Netherlands

de Laat, Jos, Royal Netherlands Meteorological Institute (KNMI), De Bilt, The Netherlands

Dell, R. L., University of Cambridge, Cambridge, United Kingdom

du Plessis, Marcel, Department of Marine Sciences, University of Gothenburg, Gothenburg, Sweden

Fogt, Ryan L., Department of Geography, Ohio University, Athens, Ohio

Fricker, Helen A., Scripps Institution of Oceanography, University of California, San Diego, La Jolla, California

Glen, E., Department of Geography, Pennsylvania State University, State College, Pennsylvania

Hancock, Alyce M., Institute for Marine and Antarctic Studies, University of Tasmania, Hobart, Tasmania, Australia

Jackson, P., Scott Polar Research Institute, University of Cambridge, Cambridge, United Kingdom

Johnson, Bryan, NOAA/OAR Earth System Research Laboratory, Global Monitoring Division, Boulder, Colorado; University of Colorado Boulder, Boulder, Colorado

Josey, Simon A., National Oceanography Centre, Southampton, United Kingdom

Keller, Linda M., Antarctic Meteorological Research and Data Center, Space Science and Engineering Center, University of Wisconsin-Madison, Madison, Wisconsin

Kittel, Chri, Department of Geography, University of Liège, Liège, Belgium; Physical Geography Research Group, Department of Geography, Vrije Universiteit Brussel, Brussels, Belgium

Kramarova, Natalya A., NASA Goddard Space Flight Center, Greenbelt, Maryland

Lait, Leslie R., NASA Ames Research Center, Moffett Field, California

Lazzara, Matthew A., Antarctic Meteorological Research and Data Center, Space Science and Engineering Center, University of Wisconsin-Madison, Madison, Wisconsin; Department of Physical Sciences, School of Arts and Sciences, Madison Area Technical College, Madison, Wisconsin

Lieser, Jan L., Bureau of Meteorology, Hobart, Tasmania, Australia; Institute for Marine and Antarctic Studies, University of Tasmania, Hobart, Tasmania, Australia

MacFerrin, Michael, Earth Science and Observation Center, Cooperative Institute for Research in Environmental Sciences (ESOC/CIRES), University of Colorado Boulder, Boulder, Colorado

MacLennan, Michelle L., British Antarctic Survey, Cambridge, United Kingdom

Massom, Robert A., Australian Antarctic Division, Australian Antarctic Program Partnership (AAPP) and Australian Centre for Excellence in Antarctic Science (ACEAS), Hobart, Tasmania, Australia

Mikolajczyk, David E., Antarctic Meteorological Research and Data Center, Space Science and Engineering Center, University of Wisconsin-Madison, Madison, Wisconsin

Milward, James, Department of Earth and Environmental Science, Temple University, Philadelphia, Pennsylvania

Mote, Thomas L., Department of Geography, University of Georgia, Athens, Georgia

Newman, Paul A., NASA Goddard Space Flight Center, Greenbelt, Maryland; University of Maryland, Baltimore County, Baltimore, Maryland

Norton, Taylor, Antarctic Meteorological Research and Data Center, Space Science and Engineering Center, University of Wisconsin-Madison, Madison, Wisconsin

Petropavlovskikh, Irina, NOAA/OAR Earth System Research Laboratory, Global Monitoring Division, Boulder, Colorado; University of Colorado Boulder, Boulder, Colorado

Pezzi, Luciano P., Laboratory of Ocean and Atmosphere Studies (LOA), Earth Observation and Geoinformatics Division (DIOTG), National Institute for Space Research (INPE), São José dos Campos, São Paulo, Brazil

Raphael, Marilyn N., Department of Geography, University of California, Los Angeles, Los Angeles, California

Reid, Phillip, Australian Antarctic Program Partnership (AAPP), Hobart, Tasmania, Australia; Bureau of Meteorology, Hobart, Tasmania, Australia

Ryan-Keogh, Thomas J., Southern Ocean Carbon-Climate Observatory, Council for Scientific and Industrial Research (CSIR), Cape Town, South Africa

Santee, Michelle L., Jet Propulsion Laboratory, California Institute of Technology, Pasadena, California

Scambos, Theodore, Earth Science and Observation Center, Cooperative Institute for Research in Environmental Sciences (ESOC/CIRES), University of Colorado Boulder, Boulder, Colorado

Schulz, Cristina, Department of Marine and Environmental Sciences, Northeastern University, Boston, Massachusetts

Shi, Jia-Rui, Courant Institute of Mathematical Sciences, New York University, New York City, New York

Souza, Everaldo, Federal University of Pará (UFPA), Belém, Pará, Brazil

Stammerjohn, Sharon, Institute of Arctic and Alpine Research, University of Colorado Boulder, Boulder, Colorado

Thomalla, Sandy, Marine and Antarctic Research Centre for Innovation and Sustainability, Department of Oceanography, University of Cape Town, Cape Town, South Africa; Southern Ocean Carbon-Climate Observatory, Council for Scientific and Industrial Research (CSIR), Cape Town, South Africa

Trusel, Luke, Department of Geography, Pennsylvania State University, State College, Pennsylvania

Wille, Jonathan D., Institute for Atmospheric and Climate Science, ETH Zürich, Zürich, Switzerland; Institut des Géosciences de l'Environnement, IRD, CNRS, Grenoble INP, Saint Martin d'Hères, France

Ziegler, Taylor, Antarctic Meteorological Research and Data Center, Space Science and Engineering Center, University of Wisconsin-Madison, Madison, Wisconsin

Editorial and Production Team

Allen, Jessicca, Graphics Support, Cooperative Institute for Satellite Earth System Studies, North Carolina State University, Asheville, North Carolina

Camper, Amy V., Graphics Support, Innovative Consulting and Management Services, LLC, NOAA/NESDIS National Centers for Environmental Information, Asheville, North Carolina

Carroll, Lauren, Content Team Lead, Communications and Outreach, NOAA/NESDIS National Centers for Environmental Information, Asheville, North Carolina

Crossman, Jacquelyn, NCEI Librarian, MPF-ZAI, NOAA/NESDIS National Centers for Environmental Information, Asheville, North Carolina

Haley, Bridgette O., Graphics Support, NOAA/NESDIS National Centers for Environmental Information, Asheville, North Carolina

Noguchi, Lukas, Technical Editor, Innovative Consulting and Management Services, LLC, NOAA/NESDIS National Centers for Environmental Information, Asheville, North Carolina

Ohlmann, Laura, Technical Editor, Innovative Consulting and Management Services, LLC, NOAA/NESDIS National Centers for Environmental Information, Asheville, North Carolina

Veasey, Sara W., Visual Communications Team Lead, Communications and Outreach, NOAA/NESDIS National Centers for Environmental Information, Asheville, North Carolina

6. Table of Contents

6. ANTARCTICA AND THE SOUTHERN OCEAN

M. N. Raphael and K. R. Clem, Eds.

a. Overview

—M. N. Raphael and K. R. Clem

In 2025, atmospheric conditions over Antarctica exhibited strong variability in pressure and temperature. Lower-than-average pressure over the continent in the early months of the year (January–March) was replaced by near-average conditions in late autumn (May–June) and winter (July–August). A strong positive Southern Annular Mode (SAM) and very strong westerlies accompanied the lower-than-average pressure in March and April, while a strong zonal wave three pattern dominated the circulation pattern offshore in winter. In spring and early summer (September–December), above-average surface pressure developed over the continent, supported by strong downward propagating positive geopotential heights from the stratosphere. This led to the development of a negative SAM supported by deep midlatitude lows over the Indian Ocean and southwest of New Zealand.

Numerous record-high monthly temperatures were set everywhere across the continent in 2025, and the polar cap saw its warmest year since the start of the record in 1979. There were no record-low monthly temperatures recorded at any station. Many regional record-high temperatures were linked to local northerly flow, predominantly associated with the zonal wave three pattern that dominated the winter circulation, influencing, for example, the Antarctic Peninsula and Dronning Maud Land where many monthly record-high temperatures were set. The most continent-wide anomalously high temperatures occurred with the above-average surface pressure that prevailed in spring.

The Antarctic Ice Sheet's surface mass balance (SMB) in 2025 saw positive anomalies, which were stronger over the grounded ice than over the floating ice shelves. The most significant anomaly occurred in April, when the Amundsen Sea Low paired with a blocking high east of the Peninsula, creating favorable conditions for sustained moisture transport, in association with a large number of atmospheric rivers into West Antarctica, some of which penetrated far inland. The resulting high snowfall rates led to the development of positive SMB anomalies both along the coast and in parts of the polar plateau.

Surface melt on the continent was above average on all the ice shelves (except the northeastern Ross Ice Shelf), particularly between mid-December 2024 and early January 2025, but was reduced to near-zero values by February. Melt on the Antarctic Peninsula approached record levels in early January. The total number of melt days generally exceeded that of the long-term average in many locations. Accompanying the melt was a record-high supraglacial meltwater presence. The strong melt was due to warmer air and ocean temperatures.

There was continued ice sheet mass loss in the West Antarctic Ice Sheet in 2025, with continued thinning of the ice sheet in the Amundsen Sea sector. The normally stable East Antarctic Ice Sheet decreased in height, with areas near the Totten ice shelf (unusually) experiencing the largest reductions. The most positive height and mass anomalies occurred along the coast of the East Antarctic Ice Sheet between March and September, while enhanced snowfall in some sectors such as the Bellingshausen Sea and Dronning Maud Land produced localized mass gains which offset the losses from the West Antarctic Ice Sheet. The anomalous snowfall in 2025 resulted in a net Antarctic mass gain of 153 Gt between January and November 2025, which was the fourth highest annual mass gain recorded by the Gravity Recovery and Climate Experiment (GRACE; since 2002).

Antarctic sea ice remained below average in 2025, with annual daily minima of sea ice extent and sea ice area recorded on 1 March, being the fourth and second lowest on record, respectively. The seasonal cycle was marked by late autumn-winter expansion and an early spring-summer retreat. This reduction in sea ice coverage led to record coastal exposure (50% more than the long-term average) throughout the year and was the net result of contrasting regional anomalies. Regionally, the Weddell Sea–Indian Ocean, Bellingshausen Sea, and central and western Ross Sea sectors experienced extremely low sea ice coverage. The opposite occurred in the eastern Ross Sea and western Amundsen Sea. The low sea ice coverage was associated with delayed sea ice advance, while higher sea ice coverage was associated with early ice advance. The net low sea ice coverage is a continuation of the trend in low sea ice extent and area seen since 2016, and in 2025 is attributed to both atmospheric and oceanic variability.

Across the Southern Ocean in 2025, sea surface temperatures exhibited positive anomalies. This continued the positive trend observed since 2005. The western Pacific region showed the greatest surface warming with peak warmth occurring in March. This was also the region with the largest positive salinity anomalies. Together with the sea surface temperatures, ocean heat content anomalies were also positive, reaching their highest level in 2025 and continuing a long-term warming trend. The increase in ocean heat content between 2024 and 2025 represents an acceleration of heat uptake by the ocean. As in 2024, chlorophyll, an important marker of ocean biogeochemistry, was at elevated levels during December 2024 and January 2025, particularly in the Atlantic. Dissolved oxygen anomalies were negative in all sectors, pointing to reduced solubility due to increased sea surface temperatures.

The 2025 Antarctic ozone hole was smaller than average, being the fourth or fifth weakest ozone hole, depending on the metric used, and among the weakest ozone holes observed since 1992. It began development in mid-July and reached its maximum size of 22.9 million km^2 on 9 September, earlier than in 2024. Further development was impeded by higher-than-average stratospheric temperatures associated with planetary scale wave events, which also contributed to the surface warming seen over the continent in spring. Observations of chlorine monoxide

Fig. 6.1. Map of weather stations and geographic regions discussed in this chapter. (Source: K. Marek, University of Wisconsin-Madison.)

were also lower than average in 2025, decreasing to near-zero by mid-October. The lower concentrations of this ozone depleting substance are part of the long-term trend of decline in ozone-depleting chlorine and bromine levels in the Antarctic stratosphere, and combined with the warm stratosphere, led to a weak ozone hole in October 2025. The ozone hole broke up on 30 November 2025, 11 days earlier than average, driven by multiple planetary-scale wave events, particularly one that began on 25 November.

More details on Antarctica's climate, weather, ice, ocean, and ozone are presented in this chapter for 2025. Unless otherwise stated, the 2025 anomalies and standard deviations are all based on the 1991–2020 climatology. Note that some sections use different climatology periods due to data availability, while others use non-traditional seasons centered around specific phenomena of interest, such as surface melt (October to April) and the Southern Ocean chlorophyll season (June to July); these details are stated at the beginning of each section. Common geographic regions and place names referenced throughout the chapter are shown in Fig. 6.1.

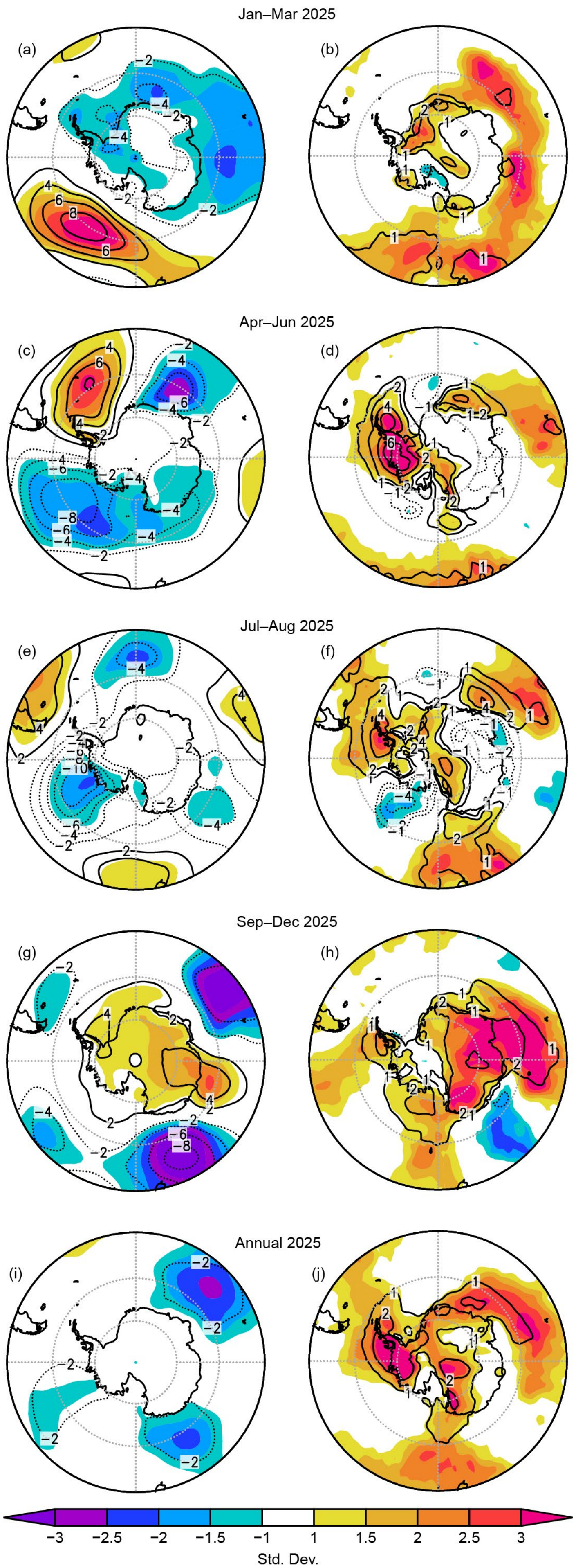

b. Atmospheric circulation and surface observations

—K. R. Clem, T. Ziegler, D. Mikolajczyk, L. M. Keller, M. A. Lazzara, S. Colwell, and R. L. Fogt

Here, the 2025 Antarctic atmospheric circulation and temperature anomalies are investigated using the European Centre for Medium-Range Weather Forecasts fifth generation atmospheric reanalysis (ERA5; Hersbach et al. 2020). Monthly surface temperature and pressure anomalies are also examined from staffed weather stations sourced from the Reference Antarctic Data for Environmental Research (READER) archive (Turner et al. 2004), and automatic weather station (AWS) data from the Antarctic Meteorological Research and Data Center (AMRDC) Data Repository (AMRDC 2022).

While various regions experienced large month-to-month variability (highlighted in the monthly anomaly plots), for brevity the ERA5 2-m temperature and surface pressure anomalies are shown grouped and averaged over four periods when the large-scale features were relatively persistent: January–March (Figs. 6.2a,b), April–June (Figs. 6.2c,d), July–August (Figs. 6.2e,f), and September–December (Figs. 6.2g,h). In addition, as reported in the Copernicus "Global Climate Highlights 2025" report based on ERA5 data (https://climate.copernicus.eu/copernicus-2025-was-third-hottest-year-record), the southern polar cap (60°S–90°S) experienced its warmest year on record in 2025 (since 1979). Thus, the 2025 annual mean anomalies are also shown in Figs. 6.2i,j. The vertical structure of the climate anomalies is examined in Fig. 6.3, showing the monthly geopotential height (Fig. 6.3a) and temperature (Fig. 6.3b) anomalies averaged over the polar cap (60°S–90°S) and the monthly circumpolar zonal wind anomalies (Fig. 6.3c) averaged over 50°S–70°S. Lastly, Fig. 6.4 shows the monthly temperature and pressure anomalies for select staffed and automated weather stations (see Fig. 6.1 for station locations and geographical references made in this section and throughout the chapter). All anomalies and standard deviations are based on the 1991–2020 climatology, with the exception of Relay Station AWS, whose

Fig. 6.2. (left) Surface pressure (hPa) and (right) 2-m temperature anomalies (°C) relative to 1991–2020 for (a),(b) Jan–Mar 2025, (c),(d) Apr–Jun 2025, (e),(f) Jul–Aug 2025, (g),(h) Sep–Dec 2025, and (i),(j) annual (Jan–Dec) 2025. Contour interval is 2 hPa for both fields with an additional ±1°C contour added for 2-m temperature; zero contours are omitted. Shading depicts standardized anomalies as indicated by the color bar at bottom. (Source: ERA5 reanalysis.)

observational record begins in 1995 (the starting year of each station's record is given in the Fig. 6.4 caption).

Continental Antarctica and the Atlantic-Indian sector of the Southern Ocean experienced generally below-average pressure during January–March, while the South Pacific was dominated by a strong ridge of high pressure (Fig. 6.2a). Locally higher cyclonic activity occurred in the southern Weddell Sea, producing strong regional warming from the coast stretching inland to parts of the plateau (Fig. 6.2b), including at Relay Station AWS, which experienced its warmest January on record (–24.9°C, 4.0°C above average; Fig. 6.4e). Enhanced cyclonic activity over much of the southern Indian Ocean was also accompanied by strong near-surface warming, but this remained offshore over the Southern Ocean. January had the strongest continent-wide warming, carrying over from December 2024 and persisting into February 2025 (Fig. 6.3b), reflecting a very warm 2024/25 austral summer over the polar cap. An intense spell of stronger-than-average circumpolar westerlies occurred during March and April (>2 m s^{-1} and 1.5 std. dev. to 2 std. dev. above average; Fig. 6.3c), accompanied by below-average tropospheric pressure over the continent (Fig. 6.3a) and strongly positive values of the Southern Annular Mode (SAM) index (bottom of Fig. 6.3); in April, Novolazarevskaya station in coastal Dronning Maud Land had its lowest April pressure on record (8.9 hPa below average; Fig. 6.4b), and the pressure at Dome C II AWS on the plateau was 10.5 hPa below average in April (Fig. 6.4d).

Over the period April–June, the atmospheric circulation became highly amplified over the Southern Ocean (Fig. 6.2c), while pressure over the continental interior returned to close to average during May–June (Fig. 6.3a). A strong ridge of high pressure developed over the South Atlantic extending westward to the Antarctic Peninsula (+6 to +8 hPa and >2 std. dev. above average), while below-average pressure formed over the South Pacific and also northeast of Dronning Maud Land. In the South Pacific-South Atlantic region, the warm, northerly flow in between the impressive low–high couplet brought record warmth to the Antarctic Peninsula extending inland to West Antarctica and the Ross Ice Shelf (Fig. 6.2d). Rothera station (on the western Antarctic Peninsula) and Marambio station (on the eastern Antarctic Peninsula) both experienced their warmest April on record (3.0°C and 8.8°C above average, respectively), and Rothera also had its warmest June on record (6.0°C above average; Fig. 6.4a). On the Ross Ice Shelf, Marble Point AWS recorded its warmest June (5.7°C above average; Fig. 6.4f). In interior West Antarctica, temperature anomalies at Byrd AWS ranged from +2.4°C in April to +4.8°C in June (not shown), but no records were set. In coastal Dronning Maud Land near the second prominent cyclonic circulation,

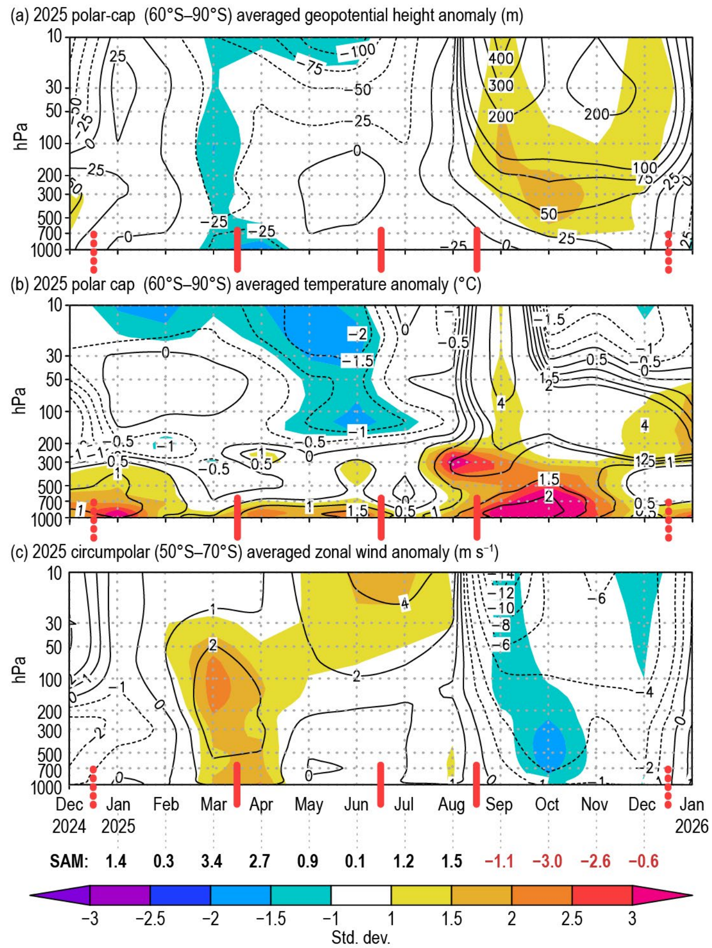

Fig. 6.3. Area-averaged (weighted by cosine of latitude) monthly anomalies over the southern polar region in 2025 relative to 1991–2020: (a) polar cap (60°S–90°S) averaged geopotential height anomalies (m; contour interval is 25 m up to ±100 m and 100 m after ±100 m); (b) polar cap averaged temperature anomalies (°C; contour interval is 0.5°C up to ±2°C and 2°C after ±2°C); (c) circumpolar (50°S–70°S) averaged zonal wind anomalies (m s^{-1}; contour interval is 2 m s^{-1} with an additional contour at ±1 m s^{-1}). Shading depicts standardized monthly anomalies as indicated by the color bar at bottom. (Source: ERA5 reanalysis.) Red vertical bars indicate the four climate periods used for compositing in Fig. 6.3; the dashed lines near Dec 2024 and Dec 2025 indicate circulation anomalies wrapping around the calendar year. Values from the Marshall (2003) Southern Annular Mode (SAM) index are shown below (c) in black (positive) and red (negative).

temperatures at Novolazarevskaya and Syowa stations ranged from 2.5°C to 4.0°C above average during April and May (Fig. 6.4b), with warm conditions persisting through July at Syowa.

During July–August, a more prominent zonal wave 3 structure developed (an offshore circumpolar band of three highs and three lows; Fig. 6.2e) while pressure over the interior continent remained close to average (Fig. 6.3a). The key regional changes were that the ridge in the South Atlantic shifted northward, and the low in the South Pacific shifted southward into the Amundsen Sea. This produced a more classic dipole temperature anomaly across West Antarctica, with strong warming over the Antarctic Peninsula and Bellingshausen Sea (a continuation of the warm conditions that began in April; Fig. 6.4a) and below-average temperatures in the Ross Sea (Fig. 6.2f). Despite the dipole, the northerly flow to the east of the cyclone channeled warmer air from the South Atlantic poleward onto the plateau (temperatures at the South Pole-Amundsen Scott station were 5.7°C above average in August; Fig. 6.4d) and down onto the Ross Ice Shelf (Marble Point AWS recorded its warmest August on record; 5.9°C above average).

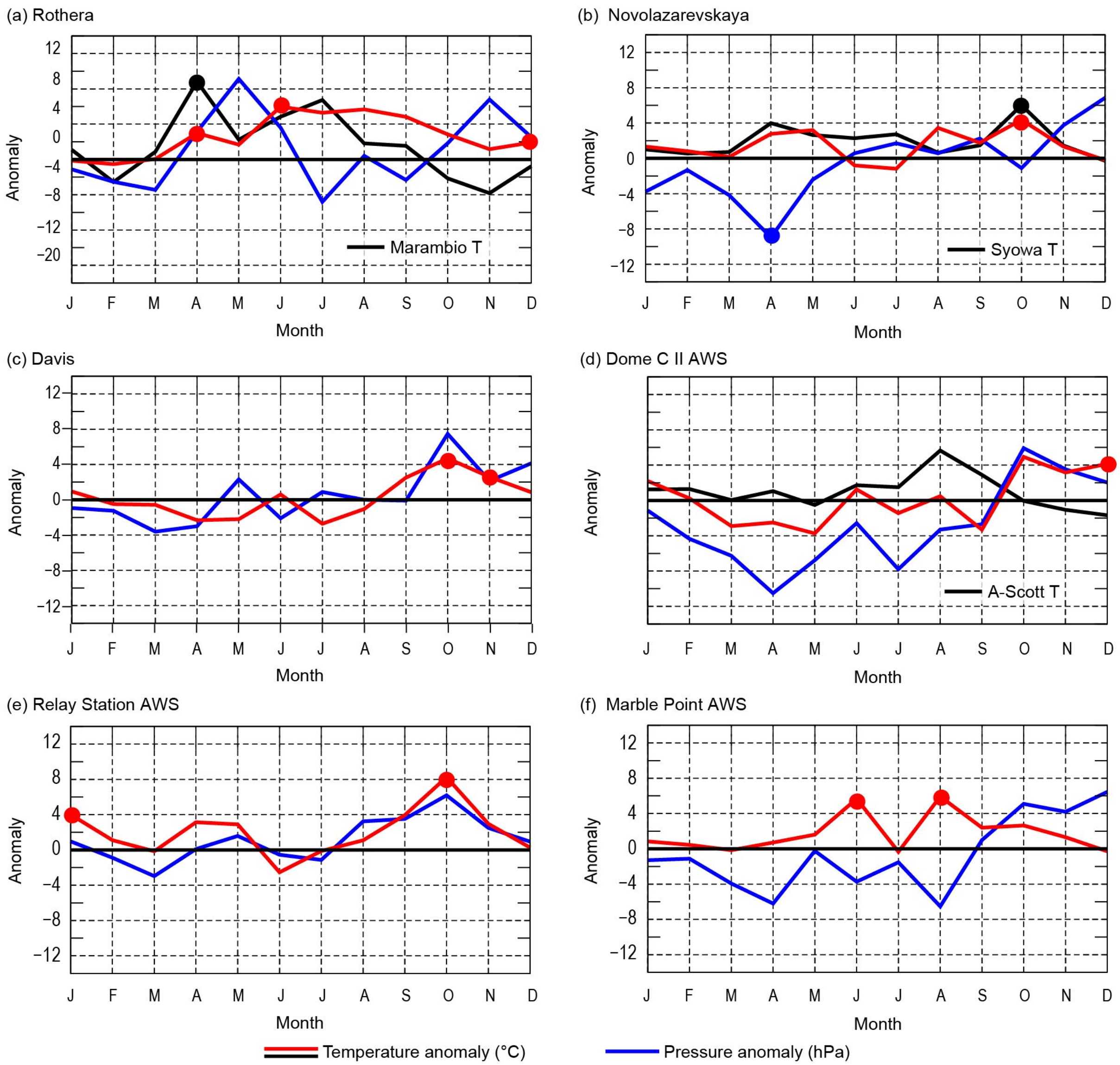

Fig. 6.4. Observed monthly Antarctic surface air temperature and station pressure anomalies during 2025 from nine representative stations [six staffed (a)–(d), and three automatic (d)–(f)]. Anomalies for temperature (°C) are shown in red and black and mean sea level pressure/surface pressure (hPa) is shown in blue. The station with both temperature (red) and pressure (blue) anomalies plotted is labeled at the top of each panel, while select complementary temperature anomalies (black) for nearby stations are labeled in the panel insets in (a),(b), and (d). Filled circles denote monthly-mean records set in 2025. The station records start in 1976 for Rothera and 1970 for Marambio in (a), 1961 for Novolazarevskaya and 1957 for Syowa in (b), 1957 for Davis in (c), 1980 for Dome C II AWS and 1957 for Amundsen Scott in (d), 1995 for Relay Station AWS in (e), and 1980 for Marble Point AWS in (f). See Fig. 6.1 for station locations.

In September, a weak positive temperature anomaly and a strong positive geopotential height anomaly (and weakening of the circumpolar westerlies) developed in the stratosphere and propagated downward to the surface in October and November, lingering into December (Fig. 6.3). A resultant strong positive surface pressure anomaly developed over the Antarctic continent, flanked by negative pressure anomalies in the middle latitudes (reflecting a negative SAM pattern, rf. SAM indices at bottom of Fig. 6.3). In particular, two very deep mid-latitude low pressure anomalies formed—one southwest of New Zealand and one in the Indian Ocean—both more than 3 std. dev. below average (Fig. 6.2g) and both aiding in transporting warm low-latitude air poleward to Antarctica. Over the continent, the positive pressure anomalies were accompanied by widespread record-setting warmth, strongest over East Antarctica and the Antarctic Peninsula (regions where the warm poleward flow was locally maximized). In October, Novolazarevskaya (4.4°C above average), Syowa (6.0°C above average), Davis (4.7°C above average), and Relay Station AWS (8.2°C above average) all set new record-high October temperatures. Davis station also had its warmest November on record (2.6°C above average), and Rothera (1.9°C above average) and Dome C II AWS (4.2°C above average) had their warmest December on record.

Annually, based on ERA5 2-m temperature averaged over the polar cap (60°S–90°S), 2025 was 1.0°C above the 1991–2020 average and the warmest year on record since 1979 (not shown). New monthly high-temperature records were set at various times of the year in nearly every region of Antarctica, including 13 new monthly high-temperature records at the nine geographically dispersed stations presented here (Fig. 6.4). While the strong positive pressure anomalies that formed in the spring played a key role in the record warmth, which appear tied to the weak stratospheric warming event (Fig. 6.3), the emergent annual-mean circulation pattern resembled a zonal wave 3 structure with three distinct negative pressure anomalies over the Southern Ocean (Fig. 6.2i). Each of these cyclonic circulations locally enhanced regional warming (Fig. 6.2j), including on the Antarctic Peninsula, where Rothera station also recorded its warmest year on record (annual average temperature of –1.4°C, 2.7°C above average; not shown), and across much of Dronning Maud Land. It is noteworthy that climate models predict a more prominent zonal wave 3 structure through the twenty-first century under anthropogenic warming (Barthélemy et al. 2026), and seven of the past eight years (2018–25) were among the eight warmest years on record based on ERA5 2-m temperature averaged over the polar cap.

c. Ice sheet surface mass balance

—L. Trusel, M. Bahrami, R. Baiman, T. Black, C. Kittel, and M. Maclennan

Surface mass balance (SMB) is the net sum of all processes that add to and remove mass from an ice sheet's surface. Over the Antarctic Ice Sheet (AIS), SMB exceeds 2500 Gt (10^{12} kg) yr^{-1} and is dominated by snowfall (Agosta et al. 2019). Sublimation and drifting snow erosion represent the largest ablation terms in the AIS SMB (van Wessem et al. 2018), given that most surface melt refreezes within the firn (Mottram et al. 2021). SMB varies strongly in space and time, exceeding 500 mm water equivalent (w.e.) yr^{-1} in high-relief coastal areas but falling below 50 mm w.e. yr^{-1} on the East Antarctic plateau (Fig. 6.5a), while peaking in autumn (March–May) and reaching a minimum in summer (December–February; Fig. 6.6a). Although only SMB on grounded ice directly affects sea level, SMB on floating ice shelves is critical for maintaining firn layer health and ice shelf stability (The Firn Symposium Team 2024). Though rare, atmospheric rivers (ARs) deliver a large fraction of AIS SMB gains (Maclennan et al. 2023; Baiman et al. 2024; Wille et al. 2025), while reduced AR activity can lead to anomalously low snowfall and a more negative mass balance (Davison et al. 2023).

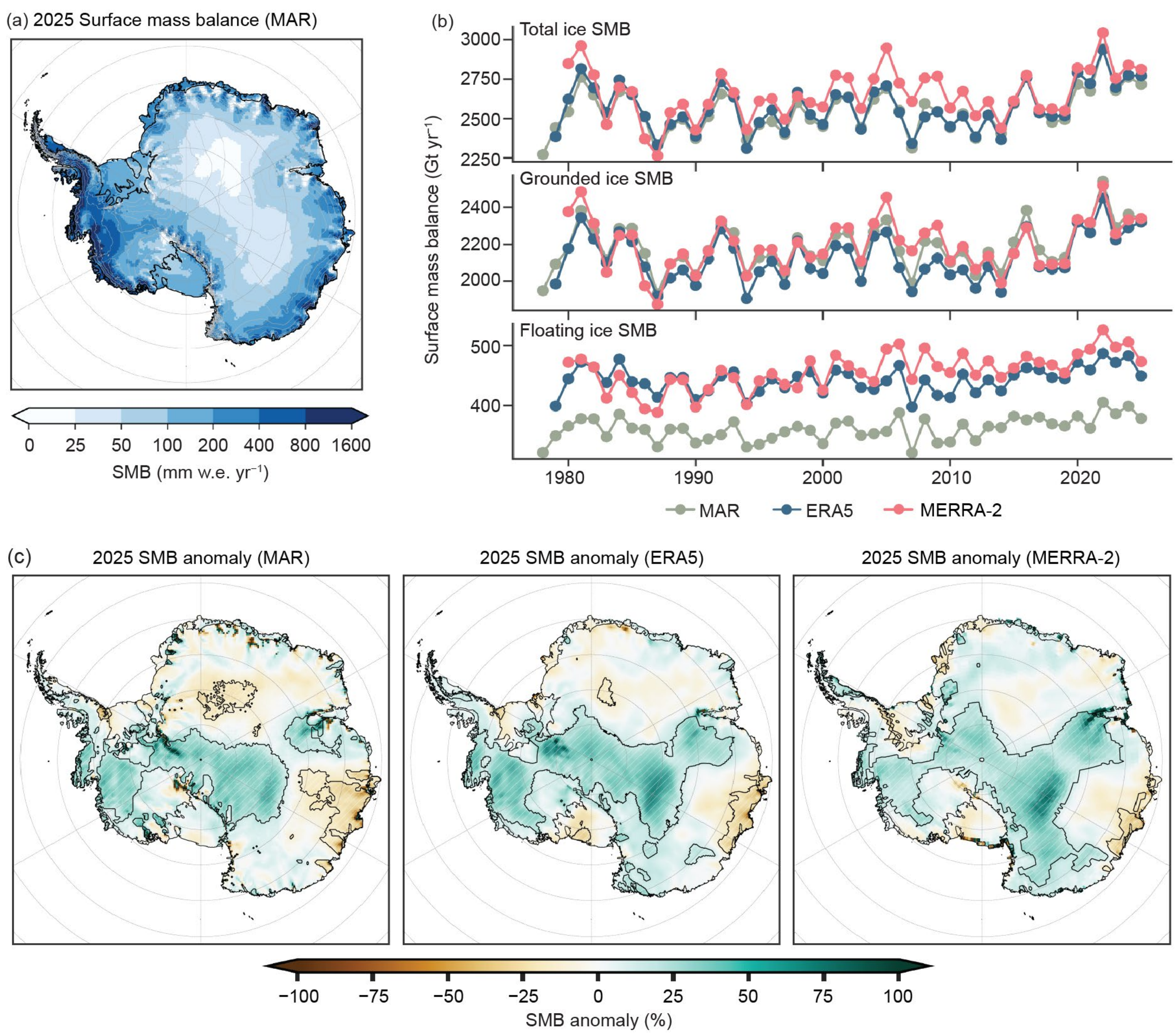

Fig. 6.5. (a) Model for Surface Mass Balance of the Arctic Ice Sheets (MAR) 2025 surface mass balance (SMB; mm water equivalent [w.e.] yr^{-1}). (b) Time series of annual surface mass balance in Gt (10^{12} kg) yr^{-1} over the full ice sheet and its grounded and floating portions. (c) Annual MAR, ERA5, and MERRA-2 SMB anomalies for 2025 relative to the 1991–2020 mean (%). The 2025 SMB anomalies are higher than the 1991–2020 std. dev. of the respective datasets in the areas outlined in black.

The 2025 SMB are estimated as total precipitation minus evaporation and sublimation (P–E) from the ERA5 (Hersbach et al. 2020) and MERRA-2 (Gelaro et al. 2017) reanalyses, and the regional climate model Model for Surface Mass Balance of the Arctic Ice Sheets (MAR) forced by ERA5, which explicitly represents SMB processes including firn evolution and meltwater runoff (Kittel et al. 2021). ERA5 and MAR have comparable spatial resolutions over Antarctica (0.25° and 25 km, respectively), both finer than MERRA-2 (0.625° × 0.5°). ERA5 (and ERA5-forced MAR) extend back to 1940, but our analysis is limited to 1979–present to avoid known pre-satellite-era biases over Antarctica (Bromwich et al. 2024). MERRA-2 begins in 1980. For spatial consistency, each dataset is bilinearly regridded to the ERA5 grid, and grounded and floating ice masks from the Antarctic Digital Database are applied (Gerrish et al. 2023). Annual and monthly SMB and ERA5 meridional moisture transport (vIVT) anomalies are computed relative to a 1991–2020 climatology. To assess synoptic drivers of SMB variability, ERA5 fields of 500-hPa geopotential height are analyzed, and the Amundsen Sea Low (ASL) position and intensity is quantified following Hosking et al. (2013). ARs are detected in MERRA-2 following Wille et al. (2021). Finally, quarterly SMB anomalies are compared with ICESat-2 ATL15 gridded rates of ice surface height change (Smith et al. 2024).

In 2025, the grounded AIS SMB equaled 2321 Gt (ERA5), 2340 Gt (MERRA-2), and 2338 Gt (MAR), representing anomalies of 1.2 std. dev. to 2.0 std. dev. above the 1991–2020 climatological means (ERA5: 2104±109 Gt yr^{-1}; MERRA-2: 2186±106 Gt yr^{-1}; MAR: 2173±98 Gt yr^{-1}). These SMBs represent the third highest in ERA5 (behind 2022 and 1981) and the fifth highest in MAR and MERRA-2. In contrast to previous years where grounded and floating SMB saw similarly strong positive anomalies, SMB over floating ice shelves was less anomalous in 2025, decreasing from 2024 according to all datasets (Fig. 6.5b), owing in part to the absence of positive SMB anomalies over the Ross and Ronne-Filchner ice shelves (Fig. 6.5c). Total and grounded SMB show a recent increase in the frequency of above-average SMB years since the early 2010s, although similarly elevated values occurred in the early 1980s (Fig. 6.5b). Including the 2025 SMB strengthens the grounded-ice SMB trend (e.g., MAR 1979–2025: 2.9 Gt yr^{-1}; $p=0.02$), but trends in all datasets remain insignificant at the 99% confidence interval and dominated by strong interannual variability. However, there are significant positive trends in floating ice shelf SMB over the full record in MERRA-2 (1.4 Gt yr^{-1}) and MAR (0.6 Gt yr^{-1}).

In contrast to the reanalyses, floating ice SMB is systematically lower in MAR both for 2025 and across the full time series (Fig. 6.5b). This offset is consistent with the fact that we quantify reanalysis SMB as P–E (e.g., Medley and Thomas 2019), whereas MAR explicitly simulates SMB, including runoff. For 2025, the MAR-ERA5 difference is ~70 Gt (MAR lower), of which ~35 Gt can be explained by runoff in MAR. The remainder likely reflects structural differences in representation of surface and boundary-layer processes between MAR and the reanalyses. We note that while runoff remains a relatively small AIS SMB term today, this discrepancy highlights why explicit firn process representation (meltwater retention and runoff; firn densification) will become increasingly important for credible ice shelf SMB projections in a warming climate (e.g., Dunmire et al. 2024).

April 2025 featured strongly positive AIS SMB (Fig. 6.6a), ranking as the highest April SMB on record in MAR and MERRA-2 and the second highest in ERA5. The synoptic pattern was characterized by an ASL that was displaced slightly east of its climatological position (Fig. 6.6b) but much deeper than average (central pressure ~1.6 std. dev. below the April climatology). This coincided with pronounced mid-tropospheric blocking east of the Antarctic Peninsula (500-hPa geopotential height anomalies up to +3.5 std. dev. above average; see Fig. 6.2c), producing a strong east–west pressure/height gradient pattern that favored sustained moisture transport into West Antarctica (Fig. 6.6b). Consistent with this circulation, April exhibited frequent episodes of anomalous poleward vIVT and a frequent occurrence of ARs (Figs. 6.6b,c), directing moisture and snowfall toward Ellsworth Land and the western Antarctic Peninsula. Precipitation was strongly orographically focused along the coastal escarpment, locally exceeding ~2 m w.e. (Fig. 6.6d). Several ARs penetrated well inland (Fig. 6.6c), helping to extend positive SMB anomalies into parts of the high elevation polar plateau (Fig. 6.6d).

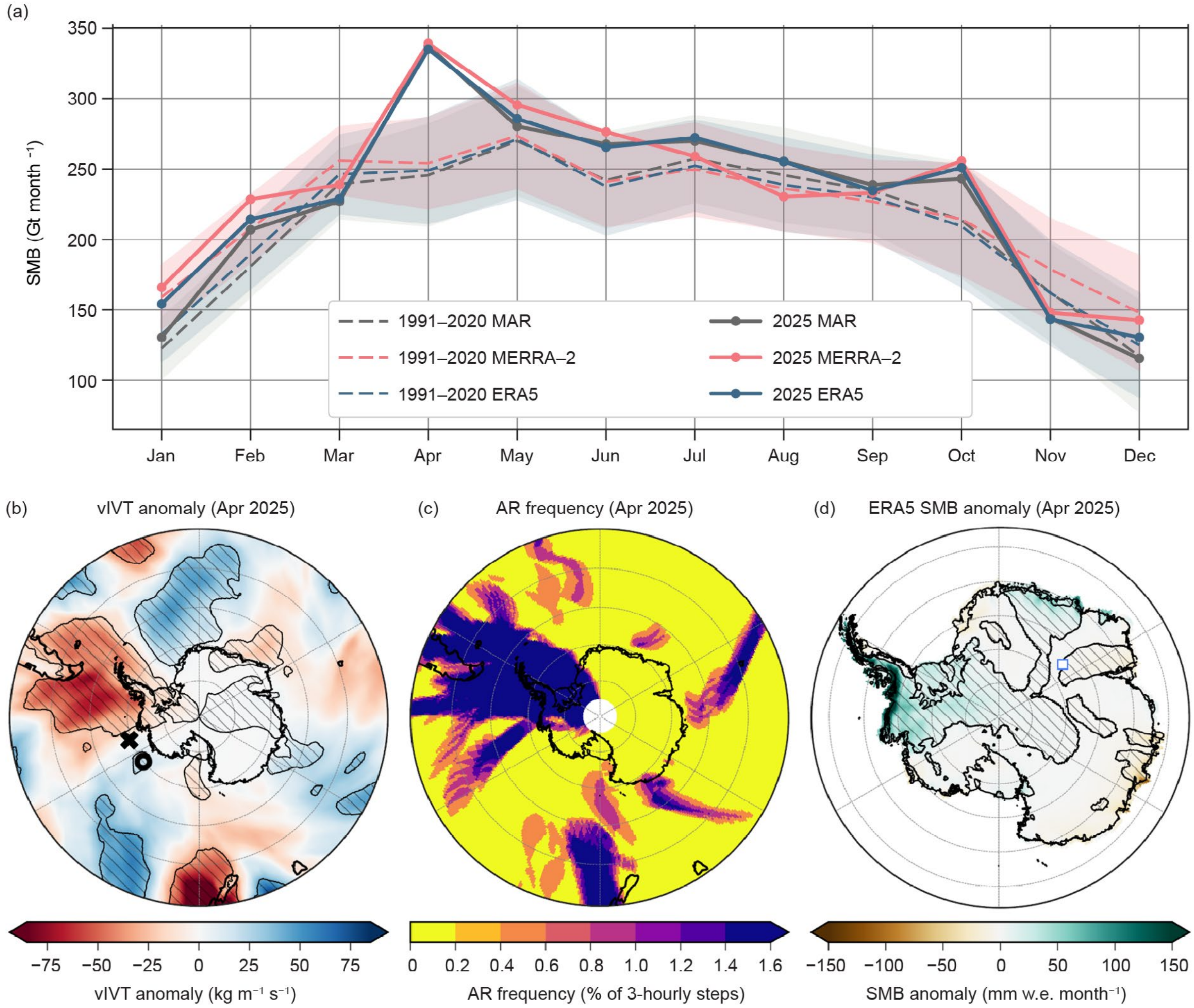

Fig. 6.6. (a) Monthly cycle of total (grounded and floating) Antarctic Ice Sheet surface mass balance (SMB) in Gt month^{-1} for the Model for Surface Mass Balance of the Arctic Ice Sheets (MAR; gray), MERRA-2 (pink), and ERA5 (blue). The 2025 values are shown with solid lines; 1991–2020 averages in dotted lines; shading indicates ±1 std. dev. (b) Apr 2025 anomalies in ERA5 meridional integrated vapor transport (vIVT) with negative values (red shades) indicating enhanced poleward moisture transport. The Apr 2025 mean Amundsen Sea Low (ASL; kg m^{-1} s^{-1}) position is marked with an X and the 1991–2020 mean position with a circle. (c) Apr 2025 atmospheric river (AR) frequency (% of 3-hr steps) from MERRA-2. (d) Apr 2025 absolute SMB anomaly (mm water equivalent [w.e.] month^{-1}) in ERA5. Outlines in (b) and (d) indicate anomalies > ±1 std. dev. relative to the 1991–2020 Apr climatology.

Finally, quarterly (91-day cycle) ATL15 estimates of surface height change (dh/dt) are compared to ERA5 SMB expressed as quarterly water-equivalent height-change rate (also see section 6e for surface height change alongside ice sheet mass balance change). There is broad spatial agreement between ERA5 SMB and ICESat-2, including coherent coastal anomaly patterns and relatively muted interior signals over the first half of 2025 (Fig. 6.7a). Notably, the effects of highly anomalous snowfall across coastal West Antarctica are revealed by positive height changes exceeding 1 m yr^{-1} for April–June 2025. A grid-cell comparison also shows a clear positive relationship between the two products (Fig. 6.7b), indicating that regions with anomalous SMB in ERA5 generally correspond to observed height changes in ATL15. In terms of magnitude, the ERA5 SMB water-equivalent dh/dt is ~40% of the ATL15 total surface dh/dt over this period, and comprises a greater percentage of the ATL15 dh/dt at snow density (e.g., ~80% at a density of 0.5 g cm^{-3}). ATL15 reflects not only SMB-driven height change but also firn processes (e.g., compaction) and potentially some residual ice-dynamic signal near fast flowing regions. Overall, this agreement provides an important, independent check that the large-scale 2025 SMB anomalies in the modeled products are physically plausible.

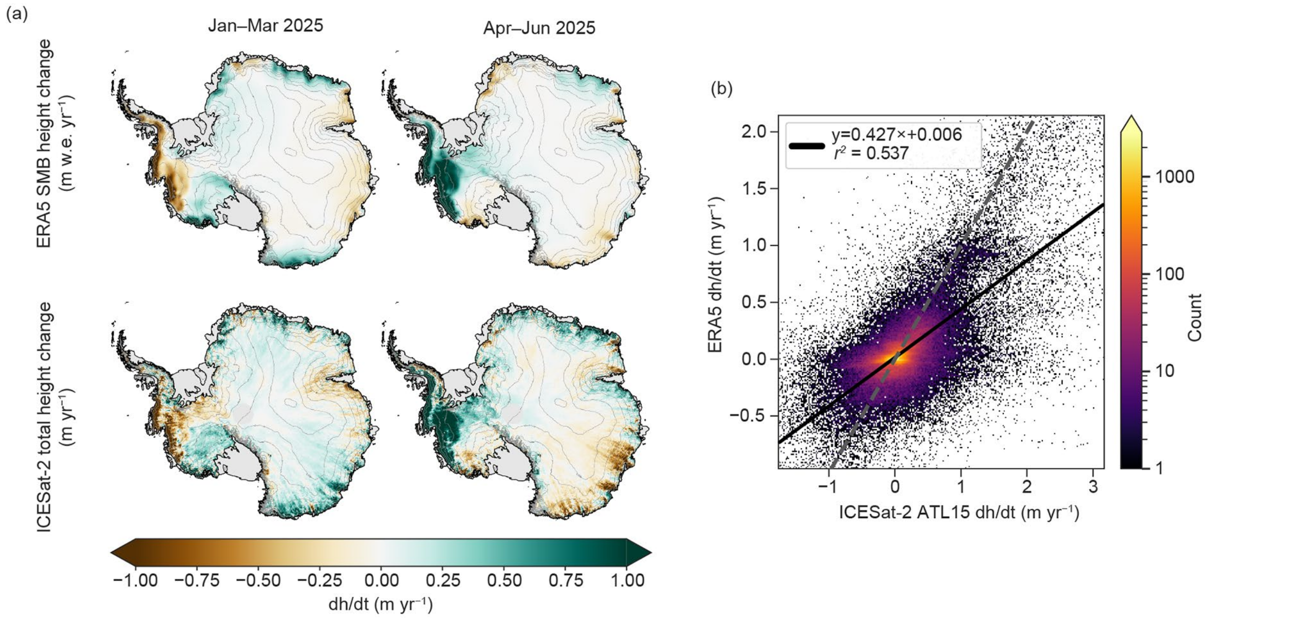

Fig. 6.7. Comparison of modeled surface mass balance (SMB)-driven height-change rates (dh/dt) from ERA5 and observed height changes (m water equivalent [w.e.] yr^{-1}) from ICESat-2 ATL15 for the first half of 2025. (a) Quarterly dh/dt (m yr^{-1}) maps showing largely coherent spatial patterns, and (b) Grid-cell ATL15 dh/dt versus ERA5 SMB water-equivalent dh/dt with colors representing point density (m yr^{-1}). The solid black line shows the best-fit regression; the dashed gray line denotes 1:1.

d. Ice sheet seasonal melt extent and duration

—M. MacFerrin, A. F. Banwell, T. L. Mote, and T. Scambos

Surface melt on the Antarctic Ice Sheet (AIS) occurs predominantly along its low-elevation coastal margins, especially on the Peninsula and on the ice shelves fringing the continent (e.g., Banwell et al. 2023). Although surface melt currently contributes only a small fraction to the overall AIS mass balance compared with snow accumulation, glacier calving, and basal melting, it is often considered to be a key measure of ice shelf stability. Meltwater that percolates into the firn and refreezes increases firn density, progressively reducing pore space and permeability. The development of near-surface impermeable layers can inhibit vertical drainage, promoting the formation of surface meltwater ponds (see Sidebar 6.1 for more details on the 2024/25 supraglacial meltwater conditions). Such ponding has been linked to ice shelf weakening and hydrofracture-driven breakup (Banwell et al. 2013); processes that may trigger upstream glacier acceleration and thinning (Scambos et al. 2014). Here, the 2024/25 Antarctic melt season is examined; the 2025/26 Antarctic melt season will be discussed in next year's report.

Daily surface and near-surface melt are mapped using satellite-derived passive-microwave brightness temperatures. The source data are distributed as daily composited polar stereographic brightness-temperatures by the National Snow and Ice Data Center (products NSIDC-0001, Meier et al. 2019 and NSIDC-0007, Gloersen 2006) spanning 1979 through the present day. Daily passive microwave brightness temperatures using the 37-GHz horizontal polarization, as well as the 37- and 19-GHz vertical polarization channels, are acquired by the Scanning Multichannel Microwave Radiometer (SMMR), Special Sensor Microwave Imager (SSM/I), and Special Sensor Microwave Imager Sounder (SSMIS) sensors aboard the NOAA Nimbus-7 and DMSP F8, F11, F13, F17, and F18 satellites. The austral melt season is defined here as 1 October through 30 April. Although small brief melt events can be measured along Antarctica's northern coastal margins throughout the year and even during the austral winter, the vast majority of melt happens during these seven months, with most melt typically occurring in December and January. An ice extent mask of 25-km grid cells for the AIS was developed from the Quantarctica v3.0 Detailed Basemap dataset (Norwegian Polar Institute 2018). All 25-km cells that contain ≥50% land ice or ice shelf are included. The AIS is divided into seven melt extent and climate regions by clustering glaciological drainage basins (based on The IMBIE Team 2020; Fig. 6.8b). The presence of liquid meltwater is determined by 37-GHz horizontally polarized brightness temperatures that exceed a dynamically established threshold each season from a simple microwave emission model that would be expected in the presence of liquid water in near-surface layers of ice and snowpack. As the melt data are binary (i.e., the algorithm indicates there is either melt or no melt); these data do not measure the intensity of the melting or the volume of meltwater present.

The method used here was first developed to track the Greenland Ice Sheet's surface melt daily (Mote and Anderson 1995; Mote 2007, 2014). Large seasonal fluctuations in passive microwave emissions from some areas of dry polar firn in Antarctica can create false positive melt indications in an unmodified version of the Greenland algorithm. This was mitigated by filtering areas that only marginally exceed the melt threshold (<10K) in the 37-GHz horizontal polarization in regions with a negative 18/19-GHz minus 37-GHz frequency gradient in the vertical polarization and has been used in previous season reports of Antarctic melt (MacFerrin et al. 2021, and each year thereafter).

Considering Antarctica as a whole, the early-to-middle portion of the 2024/25 melt season (October through January) was characterized by above-average surface and near-surface melt extent and was particularly high between mid-December 2024 and early January 2025 (Fig. 6.8b). From early February onward, melt extent declined to near-zero and remained minimal through early March. Melt was largely negligible thereafter, aside from two brief late-season spikes in early and late April.

Against this backdrop, the 2024/25 melt season was also characterized by record-high supraglacial meltwater presence, including supraglacial lakes, streams, and rivers, and based on the 2013–25 Landsat 8/9 satellite record (see Sidebar 6.1). However, above-average net snow accumulation in the 2024/25 season (section 6c) helped reduce the ice sheet's net contribution to sea level rise for the 2024/25 summer (section 6e).

Considering regional variations, the high melt extent in the early-to-mid 2024/25 melt season was observed on ice shelves in all regions except the northeastern Ross Ice Shelf (Figs. 6.8c,d). This observation contrasts to 2023/24, when only parts of the Peninsula and Maud Land and Enderby Land regions saw above-average surface melt extent, and all other ice shelf regions experienced below-average melt (MacFerrin et al. 2025).

Overall, the total number of melt days during the 2024/25 austral summer exceeded the 1991–2020 long-term average by approximately 10 days on the eastern Peninsula Larsen C Ice Shelf, 12 days to 15 days on the Fimbul Ice Shelf, and 20 days to 30 days along the eastern side of the Amery Ice Shelf. Other notable areas with above-average melt days were the North George VI, Bach, Wilkins, West, Shackleton, and Totten ice shelves.

The Antarctic Peninsula (Fig. 6.8b) saw an annual melt index of 5.55 million km^2-days, 30% above the baseline mean value of 4.28 million km^2-days. Melt extent in the Peninsula likely reached a record for the satellite era around 1–2 January 2025, with just over 50% of the ice sheet and ice shelf areas in this region showing surface melting.

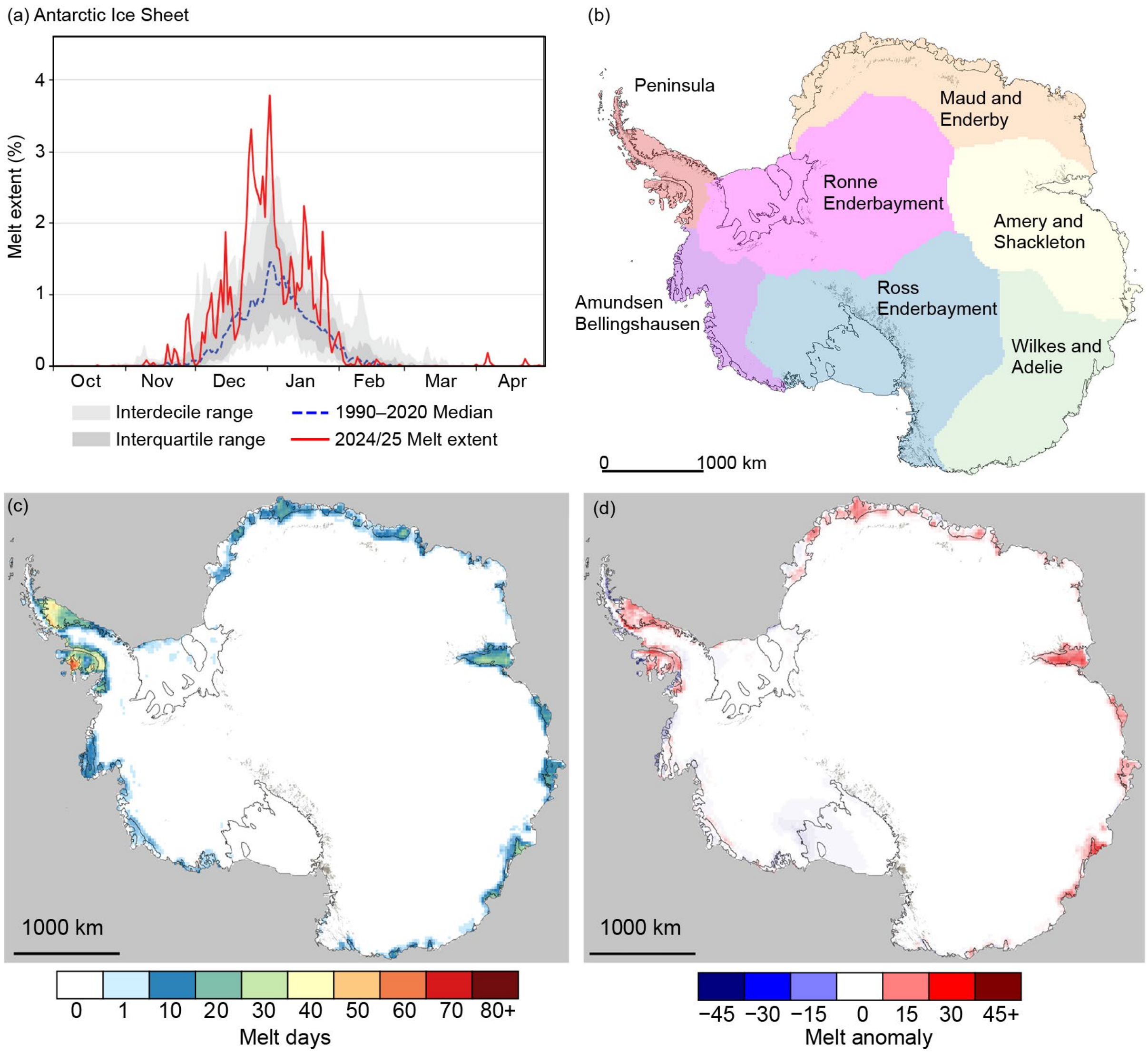

Fig. 6.8. (a) Daily surface melt extent (%; from National Snow and Ice Data Center [NSIDC]-0001, 0007) across the Antarctic Ice Sheet for the 2024/25 melt season, with 1990–2020 median values in blue and interdecile and interquartile ranges shaded in gray. (b) Reference map of Antarctic melt analysis regions. (c) Map of the sum of melt days across the Antarctic Ice Sheet in the 2024/25 melt season. (d) Map of the anomaly of the sum of melt days in the 2024/25 melt season compared to mean values from the 1990–2020 reference period.

Low air temperatures over the Antarctic Peninsula later in the melt season (section 6b) likely contributed to the observed sudden decline in melt extent and number of melt days in early February. Although air temperatures in Droning Maud Land and West Antarctica remained high relative to the average across the AIS, temperatures here rarely rose above 0°C. East Antarctica was generally cooler than average, and overall, the atmospheric circulation anomalies were not exceptional apart from a broad positive SAM pattern (see Figs. 6.2b, 6.3), indicating that the intense summer melting (and low sea ice extent, section 6f) may plausibly be attributed to broadly warmer air temperatures (and ocean temperatures, section 6g).

The first of the two late-season spikes in melt extent in early and late April was caused by a strong atmospheric river event in early April (sections 6b, 6c) moving over the eastern Pine Island Bay region and leading to local surface melting. This air mass moved eastward, bringing the tip of the Peninsula above freezing a few days later. A later event in April appears to be due to a more typical Southern Ocean cyclone that produced warm downsloping foehn winds on the eastern Peninsula ice shelves.

Sidebar 6.1: The exceptional nature of supraglacial meltwater in 2024/25

—M. BAHRAMI, E. GLEN, L. D. TRUSEL, A. F. BANWELL, P. JACKSON, AND R. L. DELL

Supraglacial meltwater, including lakes and streams, develops where near-surface firn pore space is sufficiently depleted, limiting surface melt percolation and refreezing (Kuipers Munneke et al. 2014). Once established, this water can weaken ice shelves through hydrostatic loading and hydrofracture, processes implicated in past ice shelf break-ups (Scambos et al. 2000; Banwell et al. 2013, 2019; Leeson et al. 2020). Against this backdrop, the 2024/25 melt season (November 2024–March 2025) set a record for supraglacial meltwater presence across the Antarctic Ice Sheet in the 2013–25 Landsat 8/9 satellite record (Fig. SB6.1k), highlighting potentially growing ice shelf vulnerability as warming-driven melt further reduces firn pore space (Trusel et al. 2015; Veldhuijsen et al. 2024).

Supraglacial meltwater observations during the 2024/25 melt season

A continent-wide supraglacial meltwater record was generated spanning austral summers from 2013 to 2025 using a threshold-based water classification method applied to Landsat 8/9 imagery (e.g., Moussavi et al. 2020; Tuckett et al. 2025). Here, we focus on the maximum supraglacial meltwater

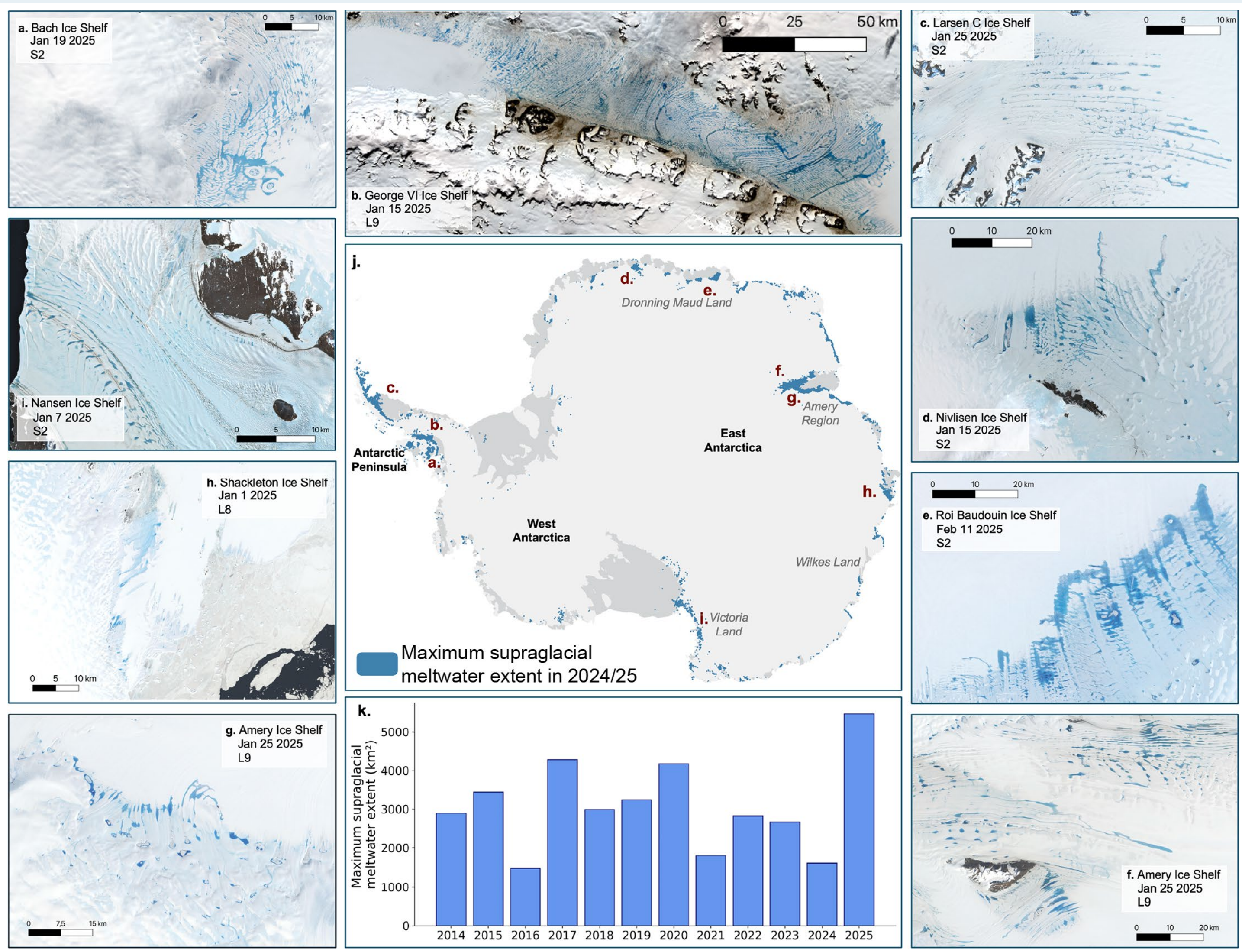

Fig. SB6.1. Supraglacial meltwater across Antarctica during the 2024/25 melt season. Representative examples of surface meltwater on ice shelves captured by Landsat 8/9 (L8, L9) and Sentinel-2 (S_2) imagery on: (a) Bach, (b) north George VI, (c) Larsen C, (d) Nivlisen, (e) Roi Baudouin, (f),(g) Amery, (h) Shackleton, and (i) Nansen. Map in (j) shows the location of each ice shelf and the maximum meltwater extent (enhanced for visualization) for the 2024/25 melt season derived from Landsat 8/9 imagery (blue). Base map of Antarctica is from Gerrish et al. (2023). Panel (k) shows maximum supraglacial meltwater extent from 2013/14 to 2024/25 based on Landsat 8/9, with the years on the x axis indicating the second year of each austral summer, i.e., 2025 corresponds to the 2024/25 season.

extent within each melt season, defined as a composite of all Landsat 8/9 water detections from November through February. Analysis of the 2024/25 melt season revealed a maximum supraglacial meltwater extent of ~5400 km^2 across Antarctica, representing the highest extent recorded since the start of the Landsat 8 era in 2013 and surpassing the previous maximum of ~4100 km^2 in 2016/17 (Fig. SB6.1k).

As in past high-melt summers, e.g., 2016/17 and 2019/20 (e.g., Banwell et al. 2021, 2023; Mahagaonkar et al. 2024; Dell et al. 2024; Arthur et al. 2022; Corr et al. 2022; Stokes et al. 2019), supraglacial meltwater in 2024/25 was mainly concentrated on the Antarctic Peninsula (AP), Dronning Maud Land (DML), and the Amery region. Across the AP, the large majority of this occurred on the north George VI Ice Shelf, which peaked at ~1127 km^2 (Figs. SB6.1b, SB6.2b), rivaling, but not surpassing, that of the 1200 km^2 reported in 2019/20 (Banwell et al. 2021), followed by Bach Ice Shelf with ~220 km^2 of meltwater area (Fig. SB6.1a). Notably, in 2024/25, meltwater ponding on George VI also occurred farther south (Fig. SB6.1b) than in previous high melt years (Banwell et al. 2021). Additional ponding was observed on inner portions of Wilkins and Larsen C ice shelves and across adjacent grounded ice (Figs. SB6.1c, SB6.2a).

Large areas of supraglacial meltwater also occurred across DML in 2024/25, reaching 1500 km^2. Approximately two-thirds of this meltwater formed on the Roi Baudouin Ice Shelf (Figs. SB6.1e, SB6.2d), with the remainder predominantly distributed across Nivlisen Ice Shelf (Fig. SB6.1d). The maximum supraglacial meltwater area in the Amery region reached ~1650 km^2 in 2024/25. Lakes occurred in Amery's eastern grounding zone, both on floating and grounded ice, along with elongated lakes across the central and southern parts of the ice shelf (Fig. SB6.2e), similar to observations in previous high-melt years (Kingslake et al. 2017; Stokes et al. 2019; Tuckett et al. 2025). Wilkes Land (325 km^2), Victoria Land (170 km^2), and Ross Ice Shelf (100 km^2) made small contributions to the Antarctic-wide total area of supraglacial meltwater, while that over Filchner-Ronne Ice Shelf (2 km^2) and coastal West Antarctica (18 km^2) was negligible.

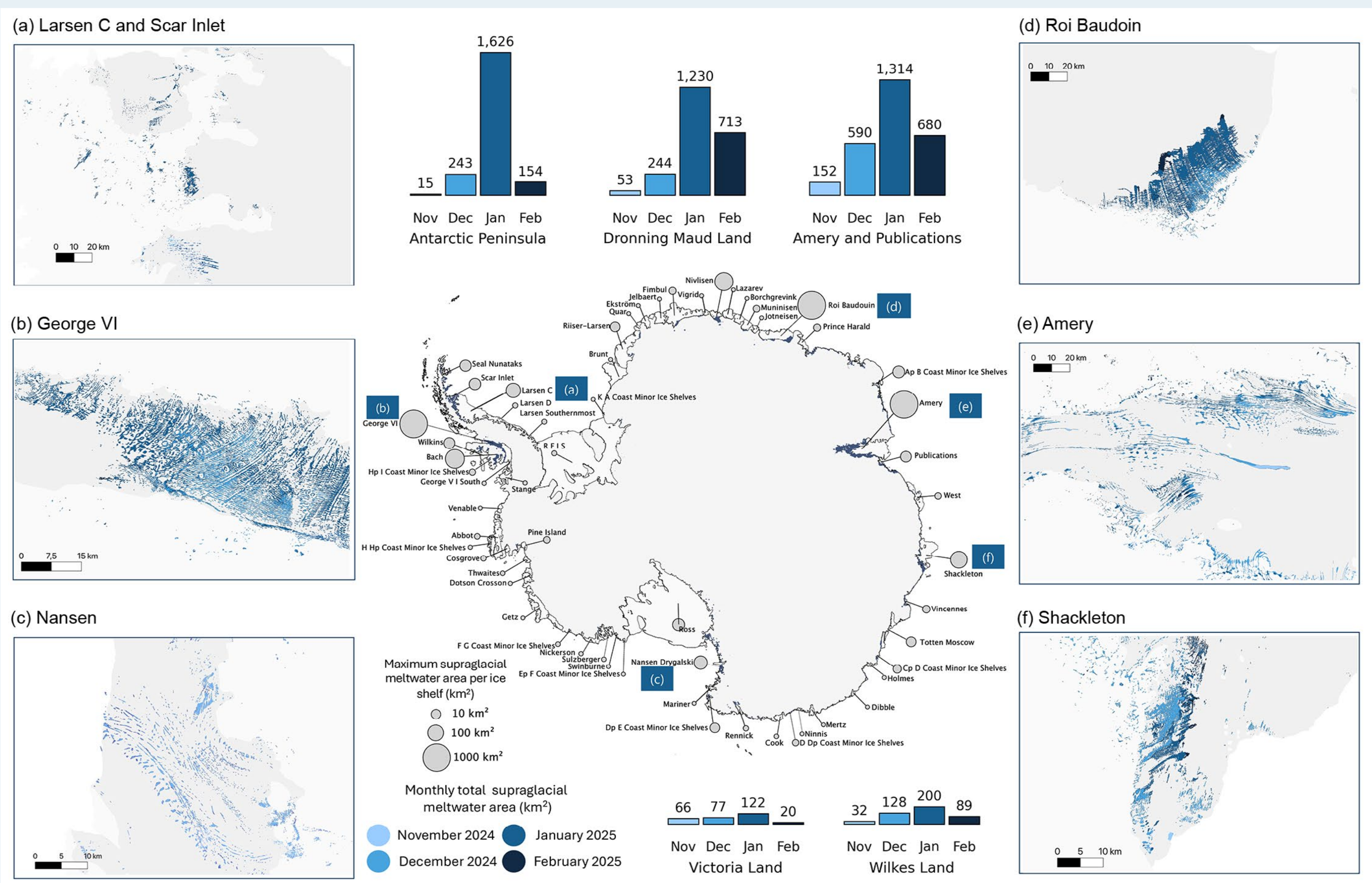

Fig. SB6.2. Antarctic-wide maximum supraglacial meltwater extent during the 2024/25 melt season and its monthly regional spatial distribution for (a) Larsen C and Scar Inlet, (b) north George VI, (c) Nansen, (d) Roi Baudoin, (e) Amery, and (f) Shackleton. Maximum 2024/25 supraglacial meltwater extent (enhanced for visualization) mapped from Landsat 8/9 imagery is shown in blue on the map of Antarctica. Circle markers are scaled by each ice shelf's maximum supraglacial meltwater area. Bar plots show the total monthly supraglacial meltwater area during the 2024/25 melt season. Panels (a)–(f) show the monthly evolution of supraglacial meltwater from Nov 2024 to Feb 2025.

The 2024/25 melt season was also characterized by active (i.e., flowing water) surface hydrological systems across multiple ice shelves. For example, a channel network on Nivlisen Ice Shelf reactivated after several years of inactivity (e.g., Dell et al. 2020), and supraglacial rivers on both Bach and Nansen ice shelves appeared to export meltwater off-shelf (e.g., Dell et al. 2026; Bell et al. 2017). Similar to previous melt years (Dell et al. 2022, 2024), widespread slush was also apparent across several ice shelves, including Roi Baudouin, Shackleton, and north George VI (Fig. SB6.1).

Potential drivers

The widespread ponding of 2024/25 reflects the combination of anomalously warm atmospheric conditions around most coastal areas during this austral summer (see Fig. 6.2b) and longer-term firn air content (FAC) depletion that has progressively reduced pore space and meltwater buffering capacity. Indeed, the largest lake coverages occur in areas where depleted FAC is reported (Banwell et al. 2021; Dunmire et al. 2024; Veldhuijsen et al. 2024).

Superimposed on this longer-term firn preconditioning, ERA5 2-m temperature anomalies (with respect to a 1991–2020 climatology) provide context for the 2024/25 conditions. The melt season began with an Antarctic-wide negative monthly temperature anomaly in November 2024 (–1.1°C) before shifting to more widespread and pronounced positive anomalies in December (+1.4°C). January 2025 recorded the strongest ice sheet-wide positive temperature anomaly in the 1979–2025 record (~+1.0°C; Fig. SB6.3a), coincident with maximum supraglacial meltwater area observed across the AP, DML, Wilkes Land, and the Amery region (Fig. SB6.2). Regionally, this peak occurred alongside temperature anomalies of around +1°C in the AP and +2°C in DML, where locally stronger anomalies reached +2.2°C in Roi Baudouin and +3.2°C in Nivlisen ice shelves, and around +2°C in the Amery Ice Shelf (Fig. SB6.3b). Anomalies remained positive in February (+0.5°C) before reducing to near-zero by March 2025.

Previous work identified a negative relationship between summer Southern Annular Mode (SAM) and meltwater area in Antarctica (Mahagaonkar et al. 2024; Tuckett et al. 2025), with negative SAM years tending to coincide with enhanced ponding. While the DJF SAM index (Marshall et al. 2003) for 2016/17 (–1.24) and 2019/20 (–0.52) is consistent with this broader pattern, the SAM was neutral (+0.05) for DJF 2024/25 (Fig. SB6.3a) and positive (+1.4) in January 2025. This indicates that the anomalously warm conditions in January 2025 occurred despite the lack of a negative SAM state that characterized previous years of elevated supraglacial meltwater extent, pointing to other mechanisms driving both anomalous warmth and lake conditions.

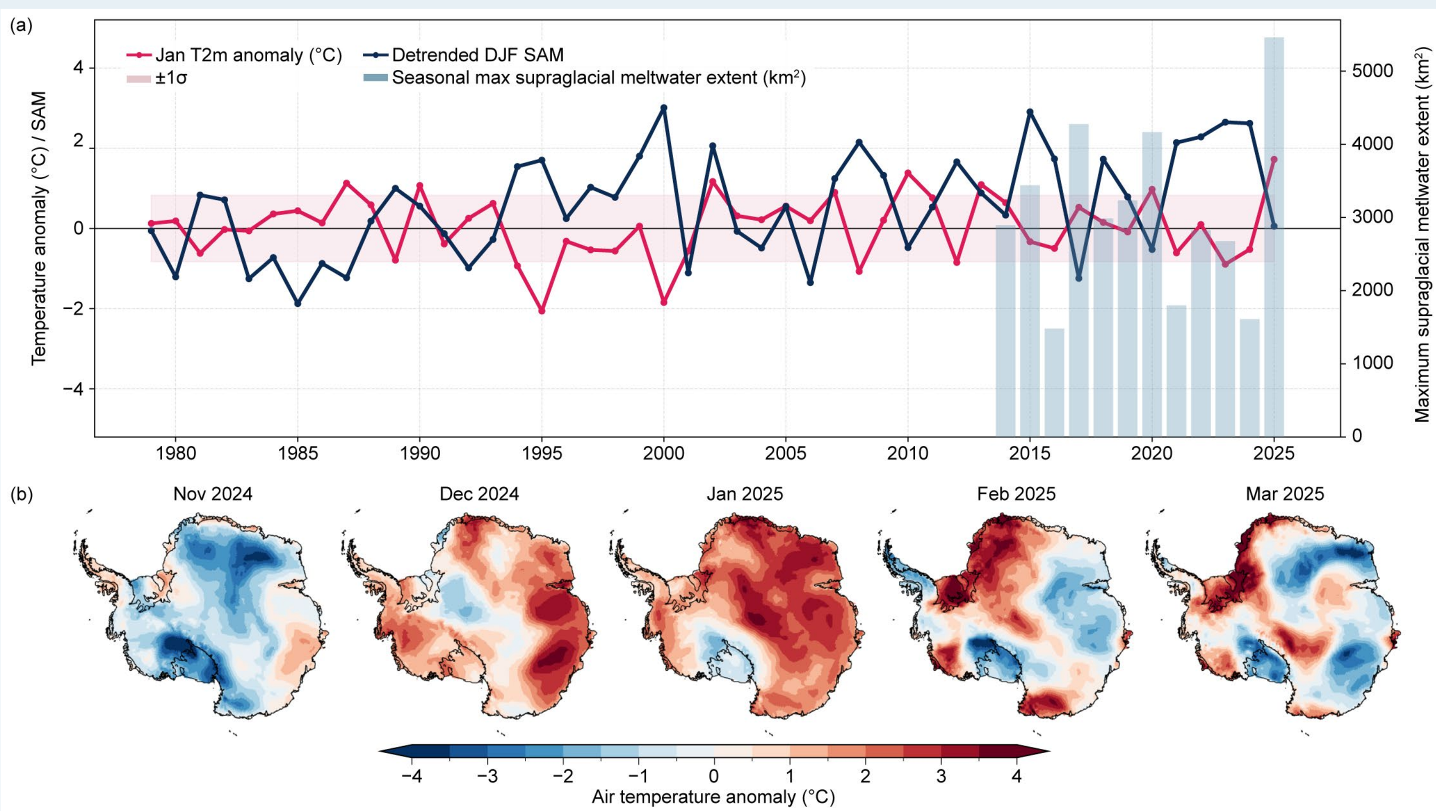

Fig. SB6.3. (a) Interannual variability for Jan 2-m temperature anomalies (T2m; °C) from ERA5 for the period 1979–2025 relative to 1991–2020 climatology (red), summer (Dec–Feb; DJF) Southern Annular Mode (SAM; blue), and maximum supraglacial meltwater extent from Landsat 8/9 (blue bars). (b) Monthly ERA5 T2m anomalies (°C). Black contours indicate ±1 std. dev. relative to the 1991–2020 climatology.

Future Outlook

Ice shelf vulnerability to surface meltwater depends both on the atmospheric forcing that produces melt and the evolving capacity of firn to buffer that meltwater. If high-melt summers became more frequent under future warming (e.g., Kittel et al. 2021), they would promote self-reinforcing expansion of surface water by lowering albedo, enhancing melt, and further reducing firn pore space, thus raising the likelihood of widespread ponding and hydrofracture where stress conditions are conducive (Bell et al. 2018).

Although runoff is a minor term in the present-day Antarctic mass budget (see section 6c), more extensive lake coverage would likely increase both lateral meltwater export as observed in 2024/25 and hydrofracture-driven vertical lake drainages (e.g., Trusel et al. 2022; Izeboud et al. 2025). Early observations from 2025/26 indicate elevated meltwater coverage across multiple regions. While it remains too early to assess whether this season will match or exceed 2024/25, the recurrence of widespread meltwater in consecutive years could represent a departure from the relatively high interannual variability that has characterized the Landsat era and move some ice shelves toward extensive lake coverages that have preceded past collapse events (Banwell et al. 2013; Leeson et al. 2020).

e. Antarctic Ice Sheet mass balance

— M. Brown, S. Adusumilli and H. A. Fricker

The Antarctic Ice Sheet (AIS) modifies global sea level through the balance between surface mass gains and dynamic mass loss of grounded ice (Otosaka et al. 2023). Surface mass gain is from snowfall accumulation, and mass loss is primarily from ice discharge across the grounding line into the floating ice shelves. Ice shelves play a critical role in slowing the rate of grounded ice flow towards the ocean, through a process called buttressing. Ice shelf mass loss, which itself does not directly contribute to global sea level, occurs through iceberg calving and basal melting. Increased ocean heat content enhances basal melting, pushing ice shelves into a negative state of balance (Adusumilli et al. 2020). This reduces buttressing and accelerates grounded ice discharge, leading to sea level rise (Smith et al. 2020; Gudmundsson et al. 2021). In recent decades, Antarctic mass loss has accelerated and exceeded ice accumulation from snowfall, but with significant variability, strengthening the need for sustained satellite-based monitoring of mass change associated with atmospheric and oceanic forcing (Fricker et al. 2025).

At the time of writing, no published estimates of total AIS height or mass change were available for 2025. Following the same approach used in previous years of this report, estimates of grounded ice surface height and mass change were derived from NASA's ICESat-2 laser altimetry and Gravity Recovery and Climate Experiment (GRACE)/GRACE-Follow On (GRACE-FO) satellite gravimetry (Clem and Raphael 2024; Raphael and Clem 2025). Only grounded ice changes are considered, as altimetry-derived height changes over floating ice shelves at sub-annual timescales remain noisy, and gravimetry cannot detect mass variations of floating ice.

Height changes were derived from ICESat-2 using measurements collected along repeated ground tracks between cycles 25 and 29, sampled at 60-m along-track resolution. These data enable estimates of annual change and three-month seasonal variability. Along-track height differences were computed between successive cycles and aggregated to produce annual (Fig. 6.9) and seasonal (Fig. 6.10) maps. Final height-change fields were smoothed using a 30-km Gaussian filter to suppress short-wavelength noise and emphasize large-scale spatial patterns.

For comparison, we also estimated mass anomalies for 2025 using satellite altimetry and gravimetry from GRACE and GRACE-FO, based on the JPL GRACE and GRACE-FO Ocean, Ice, and Hydrology Equivalent Water Height "mascon" product, Coastline Resolution Improvement (CRI)–filtered, Release 6.3 Version 4, which resolves mass variability using 300-km spherical caps (Wiese et al. 2023a). Gravity-derived mass anomalies were computed for January to November 2025 to match the ICESat-2 analysis period. Ice sheet mass anomalies were isolated by selecting mascons containing more than 10,000 km^2 of land area, as defined by the CRI land mask.

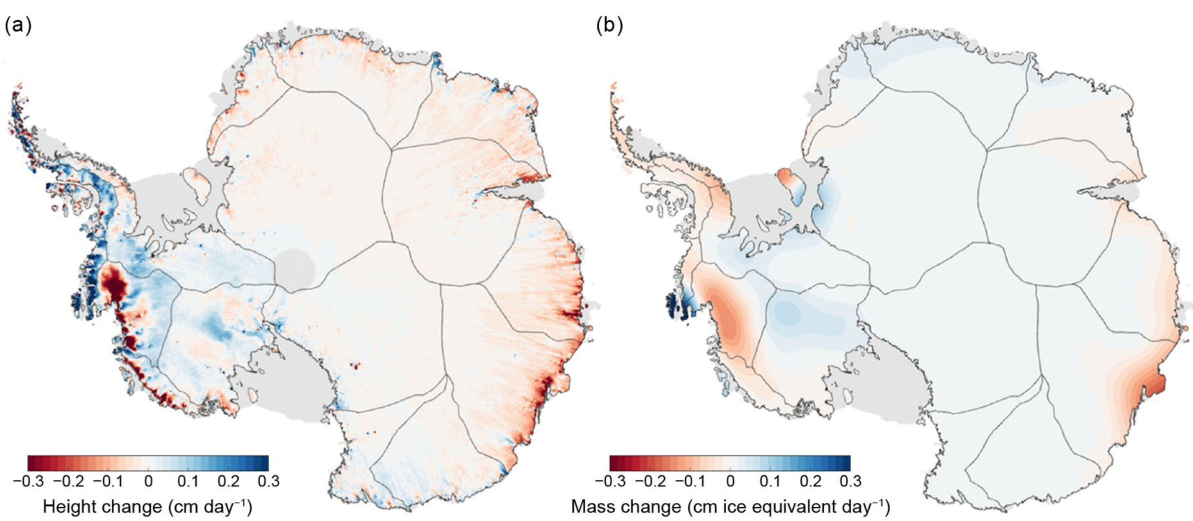

Fig. 6.9. Annual change maps for the Antarctic Ice Sheet from Nov 2024 to Nov 2025. (a) Height change (cm day^{-1}) from ICESat-2, and (b) ice equivalent mass change (cm ice equivalent day) from the Gravity Recovery and Climate Experiment Follow-On (GRACE-FO).

Area-averaged mass change rates were calculated using bilinear interpolation referenced to mascon geometric centers. Non-land regions were excluded using the BedMachine ice mask, and time series mass changes were integrated over the AIS using the Level 4 Antarctica Mass Anomaly Time Series dataset (Wiese et al. 2023b).

Maps of annual height and mass change (Fig. 6.9) reveal continued regional contrasts across Antarctica. The Antarctic Peninsula exhibits an east–west asymmetry, with surface lowering and mass loss on the eastern flank and surface rising/mass gains on the western flank. This pattern indicates differing orographic precipitation across the Peninsula during 2025, with higher precipitation on the western windward side and drier, warmer conditions on the eastern leeward side (Orr et al. 2008). This behavior was not unique to 2025 and is evident in previous versions of this report (e.g., Adusumilli et al. 2021). The West Antarctic Ice Sheet continues to experience sustained mass loss (Adusumilli and Fricker 2025). Pine Island and Thwaites glaciers maintain loss rates consistent with those observed since 2020, reflecting persistent dynamic discharge from marine-based sectors. Continued thinning, especially near grounding lines, demonstrate the ongoing dynamic ice loss due to ice–ocean processes in the Amundsen Sea sector.

The East Antarctic Ice Sheet (EAIS) experienced mean height loss of –1.26 cm in 2025, with the largest reductions concentrated near the Totten Ice Shelf. This signal departs from the historically stable or modest variability typical of most East Antarctic sectors and may reflect the

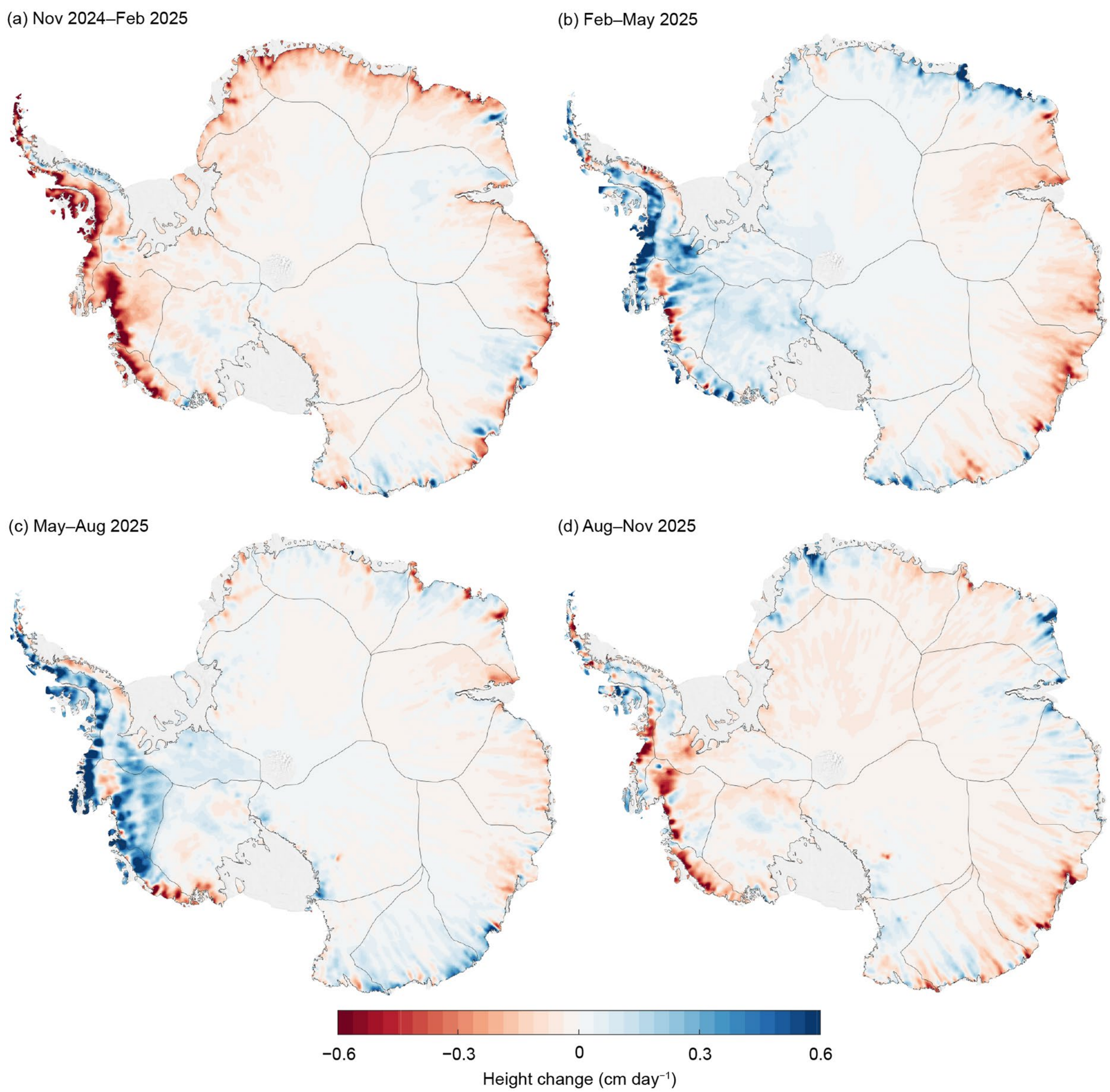

Fig. 6.10. Maps of height change from ICESat-2 shown at three-month intervals for (a) Nov 2024–Feb 2025, (b) Feb–May 2025, (c) May–Aug 2025, and (d) Aug–Nov 2025. Dates represent the central month of each three-month ICESat-2 data acquisition cycle.

below-average SMB observed in the Totten region in 2025 (Fig. 6.5) or other ice dynamics or ocean forcing. The most pronounced positive mass and height anomalies occurred between March and September, concentrated along the western coast of the EAIS. No net mass change was detected until April 2025, which started a trend linked to a 400-Gt mass gain that peaked in August before declining, yielding a net AIS annual gain of 153 Gt (Fig. 6.11). This represents the fourth-highest annual increase since GRACE observations began in 2002. The ICESat-2 three-month maps (Fig. 6.10) provide more context for these mass gains, showing that snow accumulation in the Bellingshausen Sea and Dronning Maud Land regions are responsible for offsetting the continued loss in the WAIS. And while the 2025 mass gain was dominated by anomalous snowfall, it does not reverse the long-term dynamic loss trajectory.

Instrument limitations are relevant for interpretation. Following its 2018 launch, the GRACE-FO trailing satellite (GRACE-D) experienced accelerometer degradation, and reconstructed data from the leading satellite (GRACE-C) have been used in operational products. Accelerometer measurements are sensitive to non-gravitational environmental influences, including thermospheric density variations associated with elevated solar activity during the 11-year solar-cycle peak observed in 2025. Continued integration of satellite altimetry and gravimetry remains essential for resolving short-term variability within the longer-term evolution of Antarctic mass balance and its contribution to global sea level change.

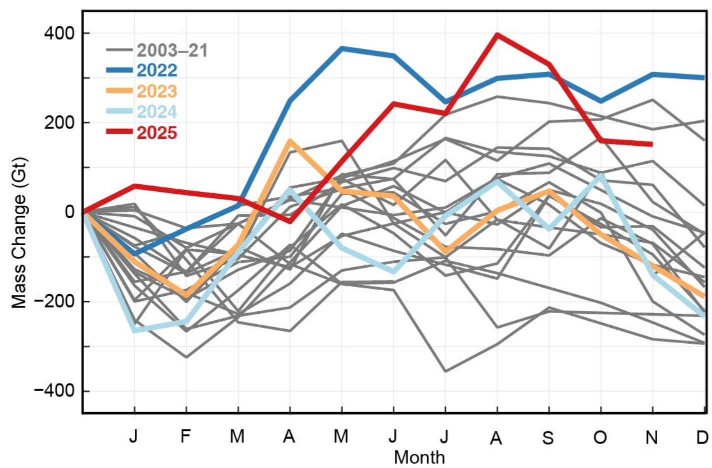

Fig. 6.11. Annual mass change (Gt) from Gravity Recovery and Climate Experiment (GRACE) and GRACE Follow-On (GRACE-FO). Time series of monthly mass changes from GRACE and GRACE-FO, with the years 2022–25 highlighted in various colors.

f. Sea ice extent, concentration, and seasonality

—P. Reid, R. A. Massom, S. Stammerjohn, S. Barreira, T. A. Scambos, and J. L. Lieser

Antarctic sea ice—formed from the freezing of seawater—is a critical component of the Southern Ocean biophysical environment and Earth's climate system. The sea ice moderates solar heating of the ocean by strongly reflecting incoming solar radiation (Riihelä et al. 2021); modulates ocean–atmosphere exchanges of heat, moisture, atmospheric gases, and momentum (Josey et al. 2024); modifies ocean properties and helps drive global ocean circulation (Meredith and Brandon 2017); protects ice shelves from potentially destructive wave action (Massom et al. 2018; Ochwat et al. 2024); and provides key habitat and food for a plethora of biota that are highly adapted to (and dependent on) its presence and seasonal rhythms (Thomas 2017).

Throughout 2025, both net Antarctic sea ice extent (SIE; Fig. 6.12a) and sea ice area (SIA; the product of SIE and concentration) were well below the long-term 1991–2020 average, except during early January. Annual daily minima of both net SIE and SIA were recorded on 1 March (1.96×10^6 km^2 and 1.21×10^6 km^2, respectively), which were fourth and second lowest on record (the record low year for both being 2023). Annual daily maximum values of net SIE and SIA were recorded on 15 and 8 September, respectively (17.85×10^6 km^2 and 13.73×10^6 km^2), with both being the third lowest on record, behind 2023 and 2024 (Reid et al. 2024). Notable features are extreme sea ice deficits in the eastern Weddell Sea–Indian Ocean sectors from March through December and year-round in the Bellingshausen Sea, which was almost ice-free until early winter. The year also included greater-than-average sea ice coverage in the eastern Ross Sea, especially in January and February. There were almost 100 days of record coastal exposure length set through the year, including the second-highest daily summertime exposure on record (13,700 km), behind 2022 (13,800 km) and almost 50% more exposure than the 1991–2020 average (Reid and Massom 2022).

The low SIE through 2025 (Fig. 6.12a) marks a continuation of the general pattern of low and record-low coverage since 2016 (Doddridge et al. 2025). In particular, and as with 2023 (Reid et al. 2024) and 2024 (Reid et al. 2025), overall sea ice seasonal growth in 2025 lagged well behind the long-term mean during the autumn-winter advance phase, which was then followed by early retreat. There is increasing evidence that changes in upper-ocean conditions, along with wind stress, may be largely responsible for the persistence in negative Antarctic SIE anomalies and reduced annual duration observed since 2016 (Cheng et al. 2022; Purich and Doddridge 2023; Maksym and Stammerjohn 2026; Silvano et al. 2025; Hobbs et al. 2026). While important, net values of SIE mask important regional and seasonal variations, and these are highlighted for 2025 below.

Five distinct periods through 2025 are identified here based on analysis of the spatiotemporal sea ice extent anomaly patterns shown in Fig. 6.12b, similar to the atmospheric seasonal analysis (see Fig. 6.2). While net SIE was close to average at the start of 2025 (Fig. 6.12a), it dipped to ~2 std. dev. below the long-term mean through March and remained 1 std. dev. to 2 std. dev. below the long-term mean throughout the year. In January through March, this net deficit was made up of several significant regional sea ice anomalies. Anomalously high SIE from ~120°W–150°W through January (i.e., 2 std. dev. to 3 std. dev. above average; Fig. 6.12a) coincided with a ridge of high pressure in the Ross-Amundsen Seas, with reduced cyclonic activity likely slowing the advection of sea ice into warmer lower latitudes where it would have rapidly melted (Himmich et al. 2024). But along the western limb of this ridge, warm northerly winds likely contributed to the anomalously low SIE over the western Ross Sea. East of the ridge, anomalously low SIE in the eastern Amundsen and Bellingshausen Seas was associated with southward advection of warm air driven by a large blocking high over the Antarctic Peninsula i.e., a likely combination of dynamic ice compaction and surface warming in January and February. The seasonal sea ice zone of the Southern Ocean is only weakly stratified, with cooler fresher waters overlying warmer much saltier waters (Pellichero et al. 2017). If the surface layer becomes less fresh (e.g., due to less seasonal sea ice melt) or the subsurface ocean becomes warmer (Wilson et al. 2026), then the upper ocean becomes even less stratified (Silvano et al. 2025), opening the door to greater upward mixing of the warm saltier waters at depth, which in turn leads to a warmer upper ocean (Spira et al. 2024), less autumn/winter sea ice production and/or greater sea ice melt in spring (see Eayrs et al. 2021, Fig. 2; Himmich et al. 2025). Unusually low SIE was also recorded in the eastern Weddell Sea, following on from well-below-average values for all of 2024 (Reid et al. 2025). Elsewhere, sea ice coverage remained close to average across East Antarctica from January through March, except in the eastern Indian and western Pacific Ocean sectors (~60°E–110°E). There, SIE was 1 std. dev. to 2 std. dev. below average, coincident with above-normal sea surface temperatures (SSTs) to the north of the ice edge (see Fig. 6.14a) that were possibly associated with southward eddy heat transfer across the ACC in the Kerguelen

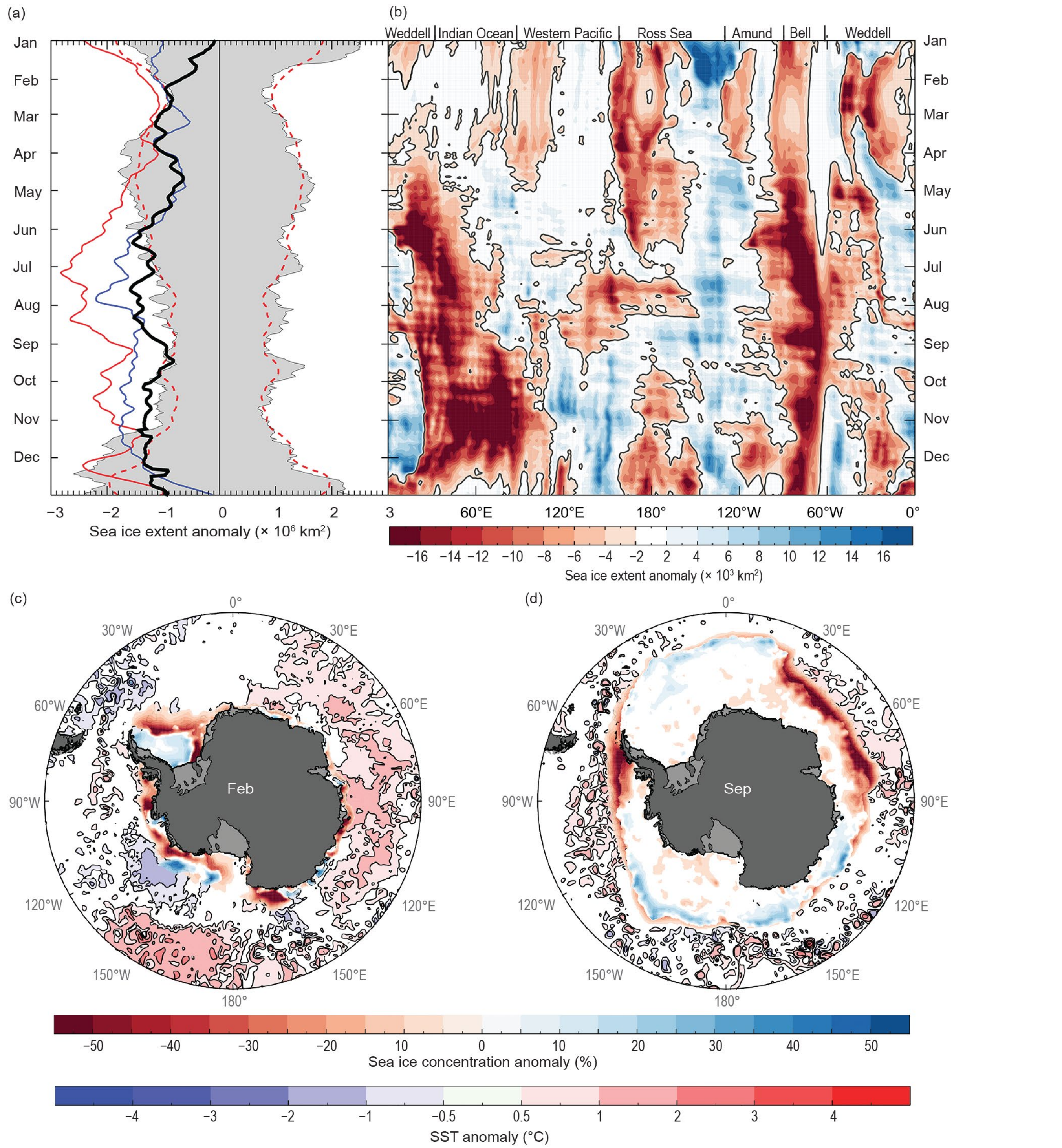

Fig. 6.12. (a) Time series of net daily sea ice extent (SIE) anomalies for 2025 (solid black line), 2024 (solid blue line), and 2023 (solid red line), based on a 1991–2020 climatology. Gray shading represents historical (1979–2023) daily SIE anomalies, red dashed line represents ±2 std. dev., and (b) Hovmöller (time–longitude) representation of daily SIE anomalies (× 10^3 km^2 per degree of longitude) for 2025. Maps of sea ice concentration anomalies (%) and sea surface temperature (SST) anomalies (°C; Huang et al. 2021) for (c) Feb 2025 and (d) Sep 2025. Sea ice concentration is based on satellite passive-microwave ice concentration data (Cavalieri et al. 1996, updated yearly and used to compute the 1991–2020 climatology and anomalies; Stewart et al. 2025 for the AMSR2 2025 sea ice concentration). See Fig. 6.1 for relevant place names.

Plateau region (Foppert 2017). Low SIE in this region has been a consistent pattern at this time of the year for the last three years.

From April through June, a general poleward intensification of low-pressure systems and a development of a high-pressure ridge in the Weddell Sea (see Fig. 6.2c) saw a change in the regional sea ice distribution pattern. Within the Weddell Sea, SIE was lower than normal, except within the central Weddell (~10°W–40°W) where SIE was higher than normal (Fig. 6.12a), possibly due to unusually strong southwesterly winds in this region (see section 6b). Farther to the east, in the western Indian Ocean sector, SIE was well below average, in conjunction with above-normal SSTs across and to the north of the ice edge. During this time, sea ice also remained low in the western Ross Sea, but advanced quickly across the eastern Ross and Amundsen Seas driven by cold southerly winds. However, farther to the east, in the Bellingshausen Sea, northerly winds exacerbated the already low sea ice conditions in that region. Across eastern Antarctica, in the southwest Pacific, sea ice coverage was close to average during these months.

July and August saw a well-defined three-wave atmospheric pattern with a deep Amundsen Sea Low (see Fig. 6.2e). This led to warm air and SST incursions into the Bellingshausen Sea and across the West Antarctic Peninsula into the eastern Weddell Sea, and into the much of the western Pacific Ocean and western Ross Sea (~120°E–180°) sectors—to suppress sea ice growth in these regions and enhance negative regional SIE anomalies through to the end of August. At this time of the year, there is typically a net eastward zonal transport of sea ice within the Weddell Sea, from 60°W through to 30°E (Kimura and Wakatsuchi 2011), and this is evident within Fig. 6.12b where positive anomalies within the central Weddell Sea advected eastward. The same zonal transport mechanism is probably also responsible for an eastward migration of negative SIE anomalies from the eastern Weddell Sea into the western Indian Ocean sector during 2025. During July and August, SIE was higher than normal in the West Pacific region (~80°E–120°E), the central Weddell Sea, and the Ross Sea (~120°W–140°W), with the latter expanding westward to 160°E during August, all associated with cold southerly winds.

From September onwards, there were regional changes in the SIE anomalies (Fig. 6.12d), driven by a weakening in the circumpolar westerly winds combined with an early September stratospheric warming (see sections 6b and 6h). Negative SIE anomalies in the eastern Weddell and southern Indian Ocean sectors during previous months expanded east into the western Pacific sector of the Southern Ocean (~20°E–110°E). The negative SIE here was perhaps enhanced by above-normal SSTs advancing across the ACC from northern latitudes in the Kerguelen Plateau region (Foppert 2017; Figs. 6.12b,d). In contrast, SIE was higher than normal in the western Pacific sector, between ~120°E and 160°E, due to the prevalence of cold southerly winds associated with the combination of an atmospheric high (~90°E–100°E) and a deep atmospheric low-pressure system centered to the west of the Ross Sea. The same low-pressure system brought warm northerly winds to the rest of the Ross Sea (to about 150°E), accelerating sea ice retreat in this region through to the end of the year. An atmospheric high-pressure system sat across the Amundsen Sea during September and October, bringing relatively calm winds and a subsequent positive SIE anomaly in the Amundsen Sea during these months. In the Bellingshausen Sea, persistently warm surface conditions since April are now reflected in the short-lived, anomalously low and already retreating winter SIE maximum in this sector.

During November, a four-wave atmospheric pattern with low-pressure centers at ~55°E, 145°E, 145°W, and 40°W (see Fig. 6.2g) significantly impacted sea ice seasonal retreat around Antarctica. Sea ice in the central-western Weddell Sea (~40°W–10°W) retreated relatively quickly, leading to negative SIE anomalies there. However, to the east of the Antarctic Peninsula and the eastern Weddell Sea, sea ice retreated slowly, influenced by cold southerly winds. The four-wave pattern also brought warm northerly winds and warmer SSTs to the Amundsen Sea, reducing the SIE in that region through to the end of the year. By the end of 2025, sea ice remained relatively highly concentrated in several regions: in the western Weddell Sea, Amundsen and eastern Ross Seas, and along the East Antarctic coastline (~130°E–160°E), with each of these regions showing some compaction of sea ice due to northerly winds.

The timings of annual sea ice advance and retreat, and resultant duration of coverage (where a sea ice year here is mid-February 2025 to mid-February 2026; Stammerjohn et al. 2008) show distinct regional anomalies (Fig. 6.13) that mirror those of the SIE (Fig. 6.12b) and SIA.

Annual sea ice advance (Fig. 6.13a) was delayed by 30 days to >60 days (compared to the 1991/92–2020/21 mean) across the Bellingshausen Sea (~60°W to ~90°W), the far eastern Weddell Sea and Indian Ocean sector (~20°E to ~60°E), along the outer ice pack of the West Pacific sector (~120°E to ~160°E), and moderately delayed (by ~15 days to 30 days) in the west-central Ross Sea (~160°E to ~160°W). Only the central-outer ice pack in the eastern Ross and western Amundsen Seas saw an appreciable early ice-edge advance (~150°W to ~115°W) by ~30 days to 60 days.

The retreat pattern (Fig. 6.13b) mostly mirrors the advance pattern where, in general, the ice-edge retreat was earlier where advance was later, and vice-versa. Notable exceptions include the broadening of exceptionally early ice-edge retreat (by 30 days to >60 days) across the entire Indian Ocean sector (~30°E to ~110°E), juxtaposed by later ice-edge retreat to the east in the Western Pacific sector (~110°E to ~160°E) where both annual advance and retreat were later than normal. Finally, the largely singular area of early ice-edge advance in the eastern Ross and western Amundsen Seas became far more attenuated in its extent, showing a much smaller area of slightly later ice-edge retreat. Taken together, the ice season duration was short across the eastern Weddell Sea and Indian Ocean, and notably also along the coastal region of the central Weddell Sea. Most of the Ross Sea and the entire Bellingshausen Sea also had a very short sea ice season. Only the western Amundsen Sea experienced a slightly longer ice season in 2025. Trends in sea ice duration (Fig. 6.13d) have changed considerably over the last few years, with smaller regions showing a trend towards a longer duration and marked increases in trends towards shorter sea ice season in the West Antarctic Peninsula–Bellingshausen Sea region by more than two days per year over the 48-year period. Another notable shorter duration trend is near ~75°E, quite possibly associated with the southward migration of warm SSTs across the ACC in this region (Foppert 2017).

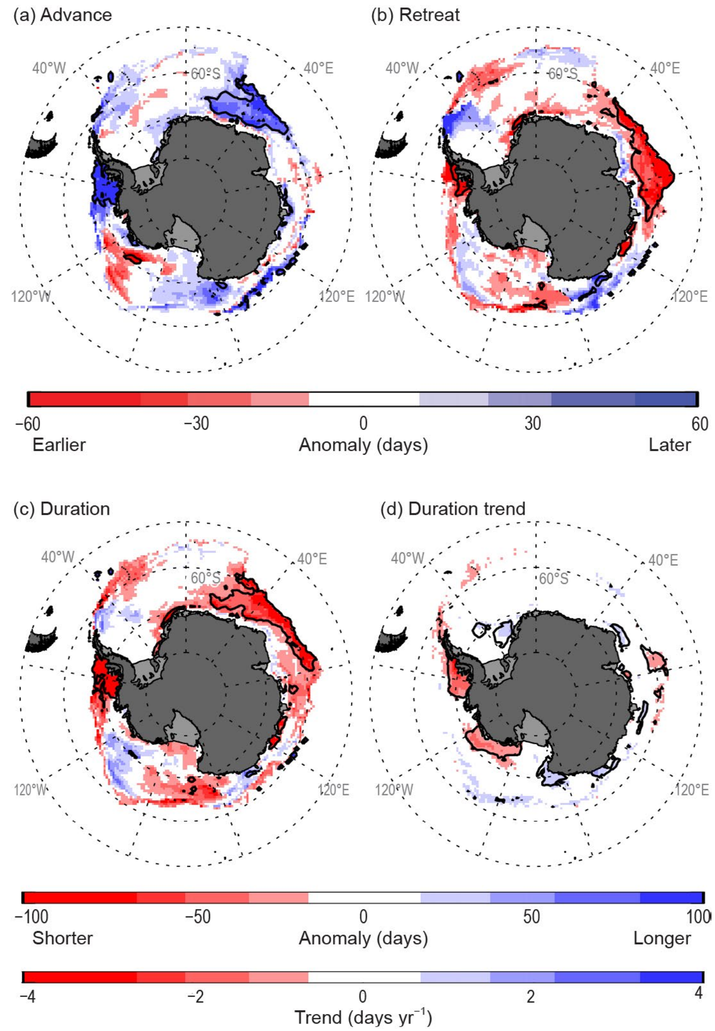

Fig. 6.13. Maps of seasonal sea ice anomaly (days) between Feb 2025 and Feb 2026 during (a) autumn ice-edge advance, (b) spring ice-edge retreat, and (c) winter ice season duration; together with (d) winter ice season duration trend (days yr^{-1}; Stammerjohn et al. 2008). The seasonal anomalies (a)–(c) are computed against the 1991/92–2020/21 climatology; the trend (d) is computed over 1979/80–2025/26. Contour lines in (a)–(c) represent where the anomalies are greater than 2 std. dev., and in (d) where the trend significance is equal to or greater than p<0.01. The 1979–2024 data are from Comiso (2023; updated yearly), while the 2025/26 data are from AMSR2 (Stewart et al. 2025); the trend is based on computed seasonal sea ice indices using the merged 1979–2024 and 2025/26 daily sea ice concentration time series.

g. Southern Ocean

—S. Thomalla, A. M. Hancock, M. Adjou, R. L. Beadling, M. du Plessis, S. Josey, Z. Kaufman, J. Milward, L. P. Pezzi, T. J. Ryan-Keogh, C. Schulz, J.-R. Shi, and E. Souza

The Southern Ocean (SO) plays a critical role in the global climate system by regulating heat and carbon exchange with the atmosphere and supplying nutrients that support ocean productivity (Frölicher et al. 2015). Here, the 2025 physical and biogeochemical state of the SO is assessed. In 2025, abnormally warm conditions prevailed, with more spatially homogenous anomalies than in recent years. Elevated air–sea heat flux anomalies across large regions of the SO indicate enhanced ocean heat uptake, which aligned with a record-setting value of upper-ocean heat content. Enhanced summer chlorophyll was observed south of the Subantarctic Front (SAF), particularly in the Atlantic. Surface dissolved oxygen anomalies were negative, consistent with warming-driven reductions in solubility. These results highlight evolving SO conditions and underscore the importance of sustained observations for tracking ongoing changes.

1. SEA SURFACE TEMPERATURE, SALINITY, AND MIXED-LAYER PROPERTIES

Sea surface temperature (SST) anomalies for 2025 (relative to a 1991–2020 climatology) were calculated from the NOAA monthly Optimum Interpolation product (Reynolds et al. 2002). Sea surface salinity (SSS) and mixed-layer depth (MLD; defined following de Boyer Montegut et al. 2004) were calculated from the Argo gridded product (Roemmich and Gilson 2009; hereafter RG09) relative to a 2004–20 climatology. As in previous years (Beadling et al. 2022; Pezzi et al. 2023; Thomalla et al. 2024, 2025), abnormally warm waters prevailed throughout most of the SO, with more spatially homogeneous anomalies, indicating coherent basin-scale warming that persisted year-round (0.4°C–0.5°C; Figs. 6.14a,b). As in 2024, surface warming was most pronounced in the western Pacific Ocean, but seasonality differed with anomalies peaking at +1.1°C (March) before weakening to near-normal conditions in November (Fig. 6.14b), whereas anomalies >+1°C persisted throughout 2024. A similar seasonal evolution was observed in the Indian Ocean with declining SST anomalies from January (~+0.7°C) to December (+0.3°C). In contrast, SST anomalies steadily intensified in the eastern Pacific Ocean from near-normal conditions in February to a maximum of ~+0.7°C in December.

In 2025, SSS anomalies exhibited both positive and negative patterns that varied regionally and seasonally (Figs. 6.14c,d). The western Pacific Ocean exhibited predominantly positive SSS anomalies, with normal conditions in March increasing to 0.11 PSU in September (Fig. 6.14d). The largest anomalies featured north of the SAF in the Atlantic and along the southern boundaries of the Atlantic and Pacific subtropical gyres (Fig. 6.14d), consistent with a gyre strengthening and enhanced poleward salt transport (Silvano et al. 2025). Consistent with 2024, all other sectors exhibited a similar seasonal cycle, but unlike the western Pacific, their summer minimum reached negative anomalies (<–0.07 PSU) before transitioning to positive anomalies from April and peaking between August and October (Fig. 6.14d).

Similar to prior years, the 2025 MLD anomaly pattern was spatially heterogeneous, with positive and negative anomalies (predominantly) north of the SAF (Fig. 6.14e). The strongest negative anomalies occurred in August (Indian), September/November (eastern Pacific), and December (Atlantic), while the western Pacific minimum anomaly occurred earlier (March) (Fig. 6.14f). Regions of negative anomalies were generally co-located with anomalously fresh and warm waters. Overall, negative anomalies were weaker in 2025 than in 2024. The strongest positive anomalies were found south of Australia in April and in November in the western Pacific.

2. AIR–SEA HEAT FLUX

The 2025 air–sea heat flux anomalies were derived from the 1991–2020 climatology using the ERA5 reanalysis (Hersbach et al. 2020). Elevated air–sea heat flux anomalies were observed across extensive regions of the western Pacific (south of New Zealand), eastern Pacific, and Atlantic, most pronounced along the Antarctic Circumpolar Current (Fig. 6.14g). The positive anomalies resulted in a SO-wide shift in ocean heat loss to heat gain during the latter half of 2025 (Fig. 6.14h). Notably, the western and eastern Pacific showed pronounced month-to-month winter variability, with basin-mean anomalies alternating by up to 40 W m^{-2} and often in opposing phase between the basins (Fig. 6.14h).

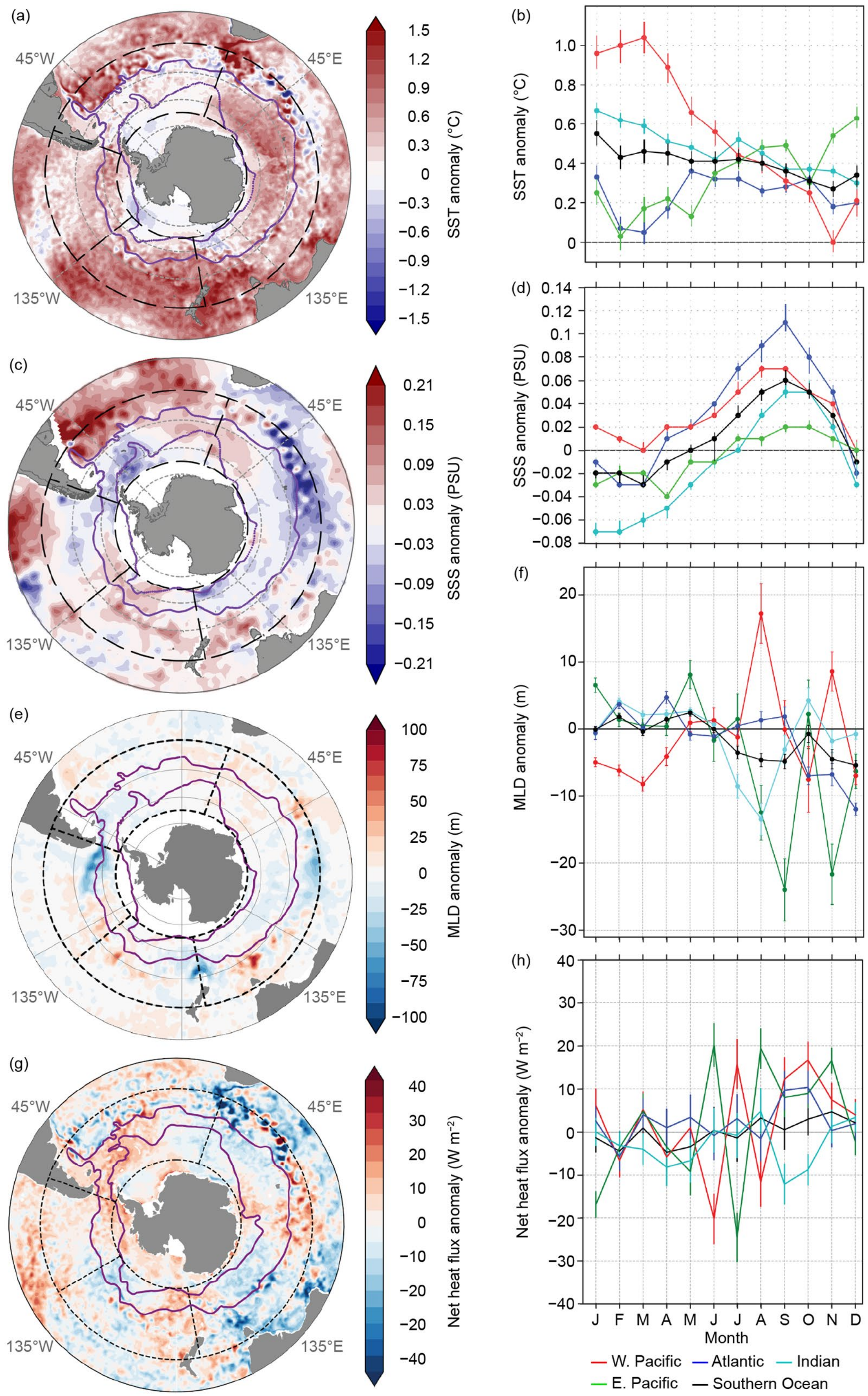

Fig. 6.14. Annual average (Jan–Dec 2025) anomalies of Southern Ocean (a) sea surface temperature (SST; °C; relative to a 1991–2020 climatology), (c) sea surface salinity (SSS; PSU), (e) mixed-layer depth (MLD; m; relative to a 2004–20 climatology), and (g) net heat flux (W m^{-2}; relative to 1991–2020 ERA5 climatology). Overlaid are the positions of the Subantarctic and Southern Boundary Antarctic Circumpolar Fronts (purple lines) defined by Orsi et al. (1995). Four distinct sectors between 40°S and 65°S are delineated by black dashed lines corresponding to the Atlantic (70°W–20°E), Indian (20°E–170°E), western Pacific (170°E–120°W), and eastern Pacific (120°W–70°W). The corresponding 2025 seasonal cycle of anomalies shown in (b) SST (°C), (d) SSS (PSU), (f) MLD (m), and (h) net heat flux (W m^{-2}) are separated according to the sectors defined above. Error bars in (b), (d), (f), and (h) represent the standard error of the climatological mean (i.e., std. dev. divided by $\sqrt{N}$, where N is the number of years in the climatology).

As in 2024 (Thomalla et al. 2025), mesoscale ocean variability left a clear imprint on air–sea fluxes north of the SAF, marked by alternating positive and negative anomalies, most evident near the Agulhas Retroflection and extending eastward into the Indian near ~40°S (Fig. 6.14g). The SO heat flux asymmetry index (Josey et al. 2023), which measures the strength of the difference in Atlantic, Indian, and Pacific sector surface heat exchange, was −0.27 in 2025, indicating that conditions were close to the climatological mean level of asymmetry for 1991–2020.

3. UPPER OCEAN HEAT CONTENT

The 0-m–2000-m upper ocean heat content (OHC) was calculated from potential temperature using the monthly gridded RG09 Argo product, with anomalies relative to the 2005–20 climatology. The 2025 OHC anomaly (Fig. 6.15a) exhibits widespread positive values, with heat gain occurring primarily north of the SAF, consistent with patterns observed in previous years (Beadling et al. 2022; Pezzi et al. 2023; Thomalla et al. 2024, 2025). Relative to 2024, OHC generally increased in 2025, while cooling occurred in the Atlantic and eastern Pacific. Based on records from the past two decades, the OHC anomaly shows a persistent long-term warming trend, reaching its highest recorded level in 2025 (Fig. 6.15b). The increase of +5.6 ZJ between 2025 and 2024 exceeds the increase of the previous two years (+4.1 ZJ and +3.2 ZJ, respectively), indicating an acceleration of heat uptake.

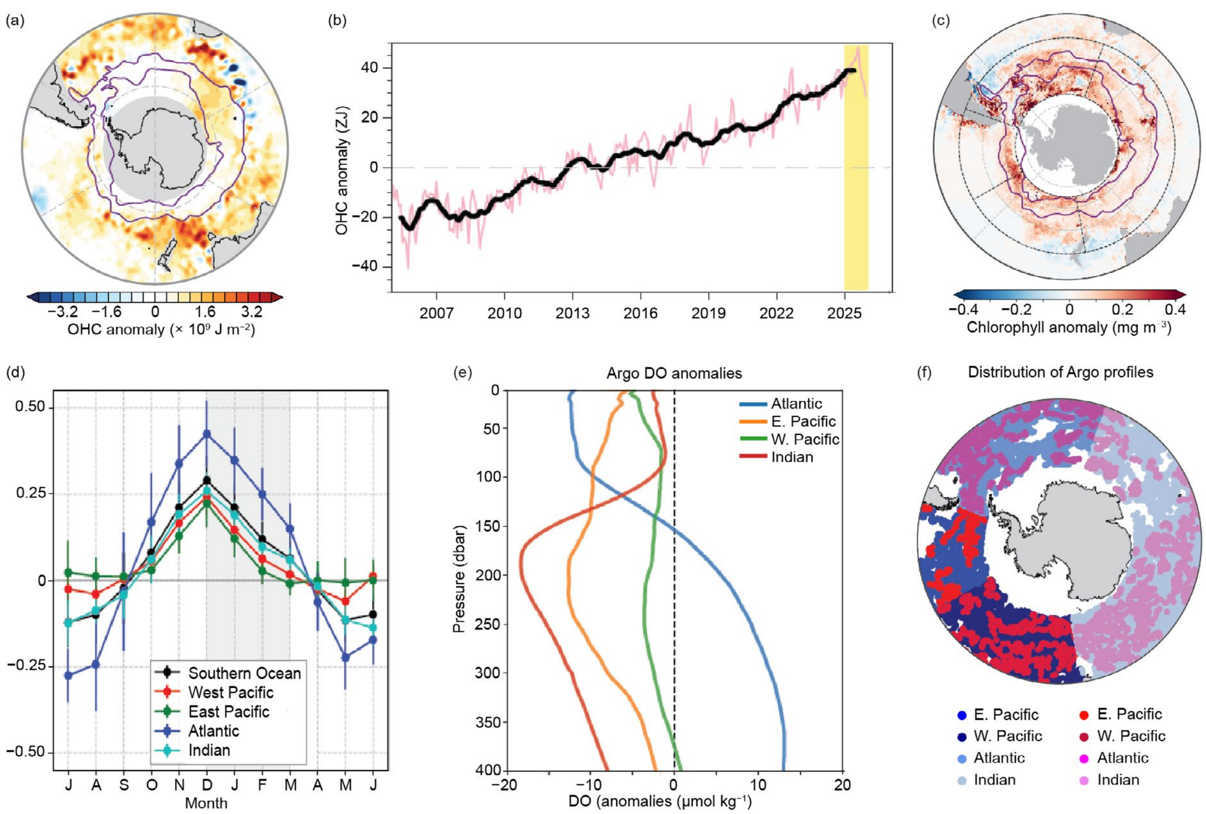

Fig. 6.15. (a) 2025 annual average ocean heat content (OHC; × 10^9 J m^{-2}) anomalies. (b) Time series of monthly average 0-m–2000-m OHC anomaly (ZJ or 10^{21} J) relative to 2004–20 Argo climatology within 40°S–65°S (red line) with 12-month running mean on top (black line) and 2025 highlighted (yellow shading). (c) Annual average (Jul 2024–Jun 2025) anomalies of eight-day, 4-km chlorophyll (mg m^{-3}) relative to 1999–2020 climatology, and (d) the 2025 seasonal cycle of anomalies for the Atlantic (70°W–20°E), Indian (20°E–170°E), western Pacific (170°W–120°W), and eastern Pacific (120°W–70°W) between 40°S and 65°S. Error bars represent the standard error of the climatological mean, i.e., std. dev. divided by $\sqrt{N}$, where N is the number of years in the climatology. Overlaid on (a) and (c) are the Subantarctic and Southern Boundary Antarctic Circumpolar Fronts (purple lines) as defined by Orsi et al. (1995). (e) Dissolved oxygen (DO) anomalies (μmol kg^{-1}) with depth (m) for Jul 2024–Jun 2025 relative to the 2004–20 Argo climatology. (f) Distribution of Argo profiles from 2004 to 2020 for the different ocean sectors (blues) relative to the distribution of profiles for the 2024/25 period (pinks and red).

4. OCEAN BIOGEOCHEMISTRY

Chlorophyll data from the eight-day (4-km) European Space Agency Ocean Color Climate Change Initiative (OC-CCI) product (v6.0; Sathyendranath et al. 2019) were processed as per Thomalla et al. (2024), with 2025 anomalies computed relative to the 1999–2020 climatology. Consistent with 2024, positive anomalies dominated south of the SAF during summer (Figs. 6.15c,d), most notably in the Atlantic, where chlorophyll concentrations were elevated. Summer anomalies were higher across all basins, with the Atlantic peaking at ~0.4 mg m^{-3} (Fig. 6.15d), nearly double that of 2024. Weaker negative anomalies occurred north of the SAF, particularly in the Atlantic downstream of South America (~−0.25mg m^{-3}) and in the Indian and western Pacific downstream of Tasmania and New Zealand (<−0.1mg m^{-3}; Figs. 6.15c,d). Dissolved oxygen (DO) anomalies (relative to the 2004–20 climatology) were derived from BGC-Argo (Wong et al. 2020) (Figs. 6.15e,f). Near-surface DO anomalies were negative in all sectors, possibly reflecting lower solubility due to increased SST. Anomalies remained negative with increasing depth in all sectors, except the Atlantic, where they were least negative near the surface (~−13 μmol kg^{-1}) and became increasingly positive from 150 m (Fig. 6.15e). Negative subsurface anomalies may reflect the spring MLD shoaling, limiting mixing with subsurface waters. While positive chlorophyll anomalies could conceivably lead to oxygen supersaturation, the largest chlorophyll anomalies occurred south of the SAF, whereas oxygen measurements used for this analysis were confined to data between 40°S and 65°S.

h. 2025 Antarctic ozone hole

—P. A. Newman, L. Coy, P. Cullis, J. De Laat, N. A. Kramarova, L. R. Lait, I. Petropavlovskikh, and M. L. Santee

The 2025 Antarctic ozone hole was smaller than average, the fourth to fifth weakest ozone hole observed since 1992. Because ozone depletion was accelerating in the 1970/80s, 2025 is compared to the mature ozone holes over the 1992-to-present period. The 2025 hole (7 September–13 October) had an average area of 18.7 million km^2 (Fig. 6.16a, magenta triangle). Against the reference period, this was the fifth smallest ozone hole on record, well below the 2006 value of 26.6 million km^2 (Fig. 6.16a, orange triangle). Other ozone hole metrics reflect this relatively weak 2025 ozone depletion. The polar ozone column minimum average (21 September–16 October) was fifth highest at 138.3 Dobson units (DU). The polar cap average (63°S–90°S; 13 September–5 October) was 246.4 DU (fourth highest). The ozone mass deficit (21 September–13 October average; the total amount of mass that is deficit relative to the amount of mass present for a value of 220 DU) was 16 million tons (fourth smallest). Together, these metrics indicate that 2025 was among the weakest ozone holes observed over the 1992–present period of severe Antarctic ozone depletion.

The day-to-day 2025 ozone hole development began in mid-July and proceeded relatively normally. The rate of ozone decline (Fig. 6.17b) was most rapid in early September, and the hole area reached a maximum of 22.9 million km^2 on 9 September (Fig. 6.17g), earlier than in recent years. Then, in mid-September, lower stratospheric temperatures (Fig. 6.17a) started to rapidly increase (section 6b) due to a series of planetary-scale wave events, which impeded further ozone hole growth. By early October, abundances of lower stratospheric ozone had stopped

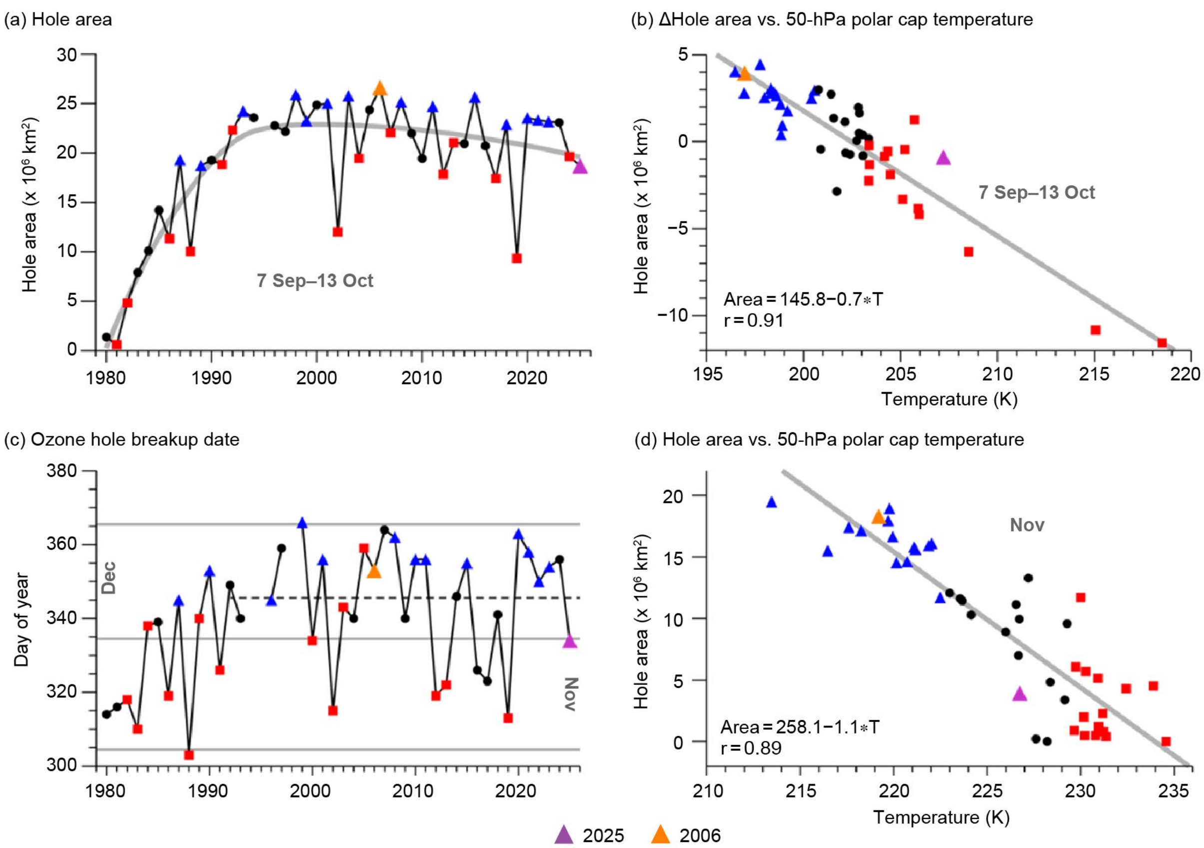

Fig. 6.16. (a) Annual 7 Sep–13 Oct average Antarctic ozone hole area (× 10^6 km^2). (b) 7 Sep–13 Oct ozone hole area anomalies vs. 7 Sep–13 Oct 50-hPa (~20-km altitude) polar cap (60°S–90°S) MERRA-2 temperatures (K). (c) Ozone hole break-up dates, where the horizontal dashed line for 11 Dec is the 1992–2024 average. (d) Nov ozone hole areas vs. MERRA-2 Nov 50-hPa temperatures. In (a), the gray curve shows a quadratic fit of effective equivalent stratospheric chlorine with a 5.2-year mean age of air (Newman et al. 2006) to the Sep hole areas (see text). Years with temperatures in the lowest (highest) third are shown as blue triangles (red squares). The years 2006 and 2025 are specifically highlighted in orange and magenta, respectively. Ozone data for 1979–92 are from Total Ozone Mapping Spectrometer (TOMS) Nimbus-7, 1993–94 are from TOMS Meteor-3, 1996–2004 are from TOMS Earth Probe, 2005–15 are from Aura Ozone Monitoring Instrument (OMI), and 2015–25 are from Suomi National Polar-orbiting Partnership (SNPP) Ozone Mapping and Profiler Suite (OMPS). The ozone hole area is the region of total column ozone values below 220 DU. There were no 1995 satellite mapper total ozone observations.

declining (Figs. 6.17b,e), leveling out at about 0.65 ppm of ozone, slightly above the 2005–24 average. Similarly, ozone in the highly depleted 12-km–20-km layer at the South Pole station had also leveled off at an above-average amount of about 40 DU (Fig. 6.17f). MLS observations of chlorine monoxide (ClO) in the vortex (Fig. 6.17d) were also lower than average in 2025 during most of the season. ClO decreased to near-zero by mid-October, ending the chemical depletion period, consistent with ozone concentrations flattening in the vortex. Compared to the extreme depletion year of 2006 (orange lines in Fig. 6.17 and orange triangles in Figs. 6.16a,b),

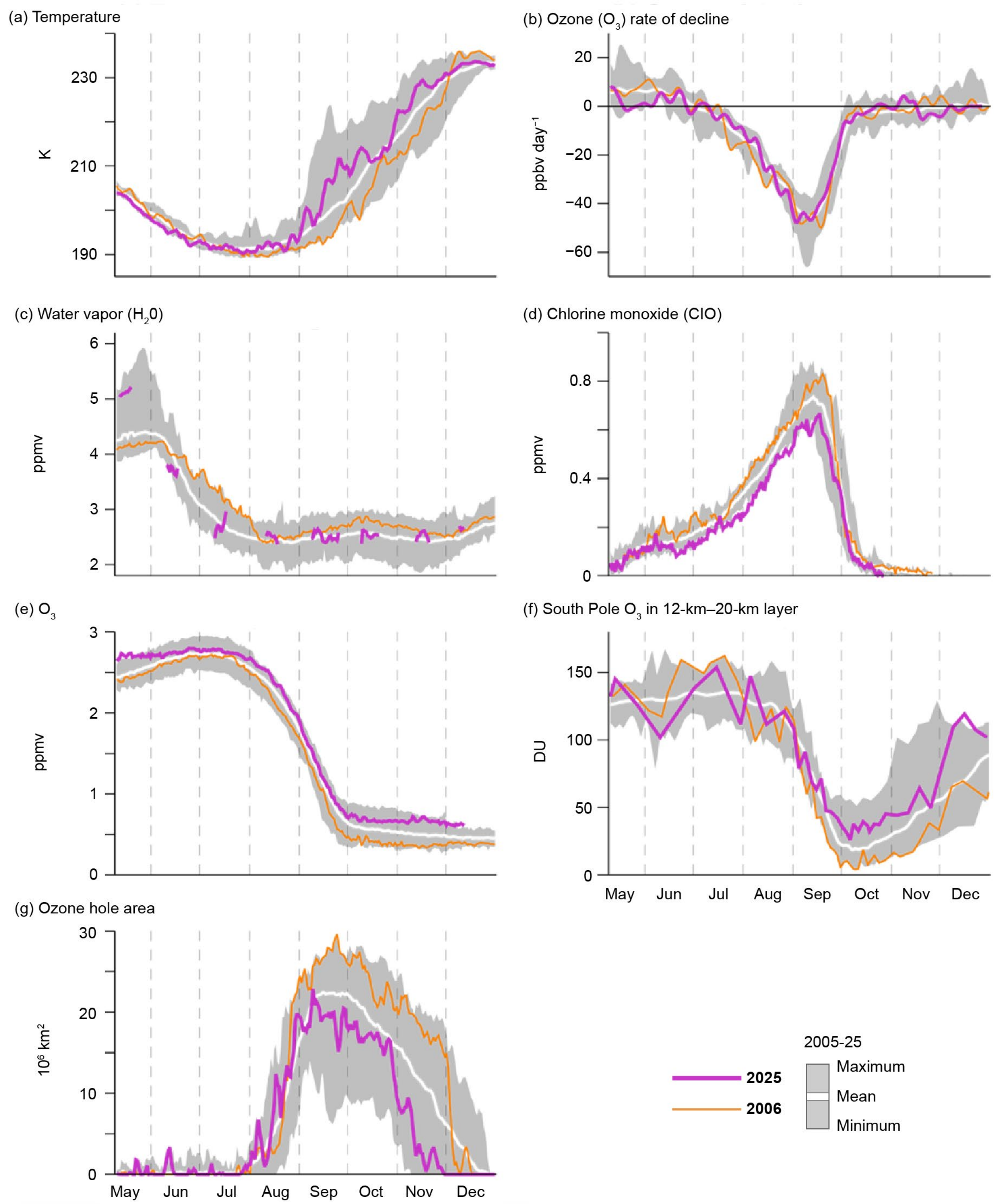

Fig. 6.17. Antarctic (a) polar cap temperature (K) at 50 hPa (~20 km, averaged 60°S–90°S) from MERRA-2. Aura MLS (updated from Manney et al. 2011) 440-K potential temperature surface (~18 km altitude) (b) ozone decline rate in the vortex (ppbv day^{-1}), (c) water vapor (H_2O; ppmv), (d) chlorine monoxide (ClO; ppbv), and (e) ozone (O_3; ppmv). (f) Lower-stratospheric ozone partial columns (12 km–20 km; DU) from South Pole ozonesondes. (g) Ozone Monitoring Instrument (OMI)/Ozone Mapping and Profiler Suite (OMPS) Antarctic ozone hole area (× 10^6 km^2; area with ozone total column less than 220 DU). The time series for 2025 (2006) is in magenta (orange). Gray shading shows daily Antarctic value ranges for 2005–24. The white lines indicate the 2005–23 long-term means.

the 2025 hole's development was less extensive than in 2006, consistent with the below-average 2025 ClO levels. This resulted in a relatively weak ozone hole by October.

The smaller-than-average austral spring depletion in 2025 is also consistent with the long-term decline of estimated chlorine and bromine levels in the Antarctic stratosphere. As noted previously, ClO values (Fig. 6.17d) were well below those in 2006 (orange line). To illustrate long-term changes in the annual ozone hole area, a quadratic regression is applied using the effective equivalent stratospheric chlorine (EESC) proxy (Fig. 6.16a). EESC is calculated using ozone depleting substance (ODS) surface observations (WMO 2022), transit times to the Antarctic stratosphere from the surface (~5.2 years), and the relative depletion efficiency of bromine with respect to chlorine (Br is ~60 more efficient than chlorine for ozone depletion). The EESC fit (gray line in Fig. 6.16a) shows a gradual 3.2 million km^2 decline in ozone hole area from 2000 to 2025.

The weak October ozone hole in 2025 is also related to higher-than-average Antarctic stratospheric temperature (Fig. 6.17a, magenta line). During the key depletion period of September to early-October, the average vortex temperature was above normal, leading to a smaller regional extent of polar stratospheric clouds (PSCs). Water vapor abundances are a key factor in PSC formation. While H_2O concentrations were elevated in May (Fig. 6.16c) due to the Hunga volcanic injection of water into the stratosphere (Millán et al. 2024), water vapor levels returned to near-normal values in August–November because of strong seasonal dehydration, also observed in 2023/24 (Santee et al. 2024; Lait et al. 2025). Polar lower stratospheric temperature is strongly correlated with ozone hole area (Fig. 6.16b). The year-to-year area anomalies in Fig. 6.16b are calculated as the difference between the Fig. 6.16a area values and the EESC gray line fit. Because the polar temperature (7 September–13 October, 60°S–90°S, 50 hPa) in 2025 was above average (Fig. 6.17a), the ozone hole area was slightly below average in 2025 (Fig. 6.16b, magenta triangle). These 2025 elevated temperatures reflect increased wave-driven warming of the Antarctic stratosphere. Both the long-term ODS decline, and above-average polar lower-stratospheric temperature led to a weak 2025 ozone hole.

The ozone hole broke up on 30 November 2025 (Fig. 6.16c, magenta triangle). The breakup is estimated by calculating when the ozone hole area falls to zero (Fig. 6.17g). The ozone hole area rapidly declined to 18.9 million km^2 by 14 September, with a slower decline to 16.9 million km^2 by 20 October. The ozone hole underwent two intervals of rapid decline in late October and mid-November. Such rapid declines are driven by planetary-scale wave events originating in the troposphere and lower-most stratosphere. These wave events deposit easterly momentum in the stratosphere that decelerates the polar vortex, warms the polar lower stratosphere by inducing a downward flow, and mixes ozone-rich air masses into the polar region. There were five significant wave events (not shown) during the 2025 austral spring that warmed the vortex. Most importantly, the wave event of 16 September 2025 largely ended the rapid ozone depletion period. The hole had considerably shrunk by early November (Fig. 6.17g) and vortex temperatures remained high because of the multiple wave events (Fig. 6.16d, magenta triangle, and Fig. 6.17a). The 30 November hole breakup was 11 days earlier than the 1992–2024 average (Fig. 6.16c, dashed line), accelerated by a wave event that began on 25 November. The greater wave activity in the September–November 2025 period led to the earlier-than-average 2025 ozone hole breakup.

Acknowledgments

- K. R. Clem and M. N. Raphael would like to extend a very warm thank you to Kathryn Marek, Antarctic Meteorological Research and Data Center, Space Science and Engineering Center, University of Wisconsin-Madison, for producing the map in Fig. 6.1.
- Work at the Jet Propulsion Laboratory, California Institute of Technology, was done under contract with the National Aeronautics and Space Administration (NASA). Support was also provided by the NASA Modeling and Analysis Program. We are indebted to the many NOAA Corps Officers and GML technical personnel who spend the winters at South Pole Station to obtain the ongoing balloon and ground-based data sets. We also acknowledge the logistics support in Antarctica provided by the National Science Foundation Office of Polar Programs.© 2024. All rights reserved.
- P. Reid and J. Lieser were supported through the Australian Bureau of Meteorology, and R. Massom by the Australian Antarctic Division. P. Reid and R. Massom were supported by the Australian Government as part of the Antarctic Science Collaboration Initiative program (Project Number ASCI000002). For R. Massom, this work was also supported by the Australian Research Council Special Research Initiative the Australian Centre for Excellence in Antarctic Science (Project Number SR200100008).
- S. Stammerjohn was supported under NSF PLR–1552226; she also thanks the Institute of Arctic and Alpine Research and the National Snow and Ice Data Center, both at the University of Colorado Boulder, for institutional and data support.
- The Southern Ocean Observing System (SOOS) is a joint international initiative of the Scientific Committee on Antarctic Research (SCAR) and the Scientific Committee on Oceanic Research (SCOR). L. P. Pezzi acknowledges support from PROANTAR's Antarctic Modelling and Observation System (ATMOS 2) Project under the CNPq/PROANTAR award 440848/2023-7 and PQ 303981/2023-7. R. L. Beadling, J. Milward, and Z. Kaufman were supported under the NSF Division of Polar Programs Grant NSF2319828. S. Thomalla is supported through the CSIR's Southern Ocean Carbon-Climate Observatory (SOCCO) Programme (http://socco.org.za/) funded by the Department of Science and Innovation (DSI/CON C3184/2023), and the CSIR's Parliamentary Grant (0000005278).
- L. P. Pezzi acknowledges support from PROANTAR's Antarctic Modeling and Observation System (ATMOS 2) Project under the CNPq/PROANTAR award 440848/2023-7 and PQ 303981/2023-7.
- R. L. Beadling and J. Milward were supported under the NSF Division of Polar Programs Grant NSF2319828.
- S. Thomalla and T. J. Ryan-Keogh were supported through the CSIR's Southern Ocean Carbon-Climate Observatory (SOCCO) Programme (http://socco.org.za/) funded by the Department of Science and Innovation (DSI/CON C3184/2023), the CSIR's Parliamentary Grant (0000005278) and the National Research Foundation (SANAP23042496681; MCR210429598142).
- T. Ziegler, M. A. Lazzara, D. Mikolajczyk, and L. M. Keller acknowledge support from the National Science Foundation, Grant Numbers 195120, 1951603, and 2301362.

Appendix 1: Acronyms

AAPP	Australian Antarctic Program Partnership
AIS	Antarctic Ice Sheet
AMRDC	Antarctic Meteorological Research and Data Center
AP	Antarctic Peninsula
AR	atmospheric river
ASL	Amundsen Sea Low
AWS	automatic weather station
ClO	chlorine monoxide
CRI	Coastal Resolution Improvement
DML	Dronning Maud Land
DMSP	Defense Meteorological Satellite Program
DO	dissolved oxygen
DOISST	Daily Optimum Interpolation Sea Surface Temperature
DU	Dobson unit
EAIS	East Antarctic Ice Sheet
EESC	effective equivalent stratospheric chlorine
FAC	firn air content
GRACE	Gravity Recovery and Climate Experiment
GRACE-FO	Gravity Recovery and Climate Experiment Follow-On
IMAS	Institute for Marine and Antarctic Studies
IMBIE	Ice Mass Balance Intercomparison Exercise
MAR	Model for Surface Mass Balance of the Arctic Ice Sheets
MLD	mixed-layer depth
MLS	Microwave Limb Sounder
NASA	National Aeronautics and Space Administration
NSIDC	National Snow and Ice Data Center
OC-CCI	Ocean Colour Climate Change Initiative
ODS	ozone depleting substance
OHC	ocean heat content
OMI	Ozone Monitoring Instrument
OMPS	Ozone Mapping and Profiler Suite
PSC	polar stratospheric cloud
S2	Sentinel-2
SAF	Subantarctic Front
SAM	Southern Annular Mode
SCAR	Scientific Committee on Antarctic Research
SIA	sea ice area
SIE	sea ice extent
SMB	surface mass balance
SMMR	Scanning Multichannel Microwave Radiometer
SNPP	Suomi National Polar-orbiting Partnership
SO	Southern Ocean
SOCCO	Southern Ocean Carbon-Climate Observatory
SOOS	Southern Ocean Observing System
SSM/I	Special Sensor Microwave Imager
SSMIS	Special Sensor Microwave Imager Sounder
SSS	sea surface salinity
SST	sea surface temperature
TOMS	Total Ozone Mapping Spectrometer

vIVT	vector-invariant water transport
WAIS	West Antarctic Ice Sheet
WMO	World Meteorological Organization

Appendix 2: Datasets and sources

Section 6b Atmospheric circulation and surface observations

Sub-section	General Variable or Phenomenon	Specific Dataset or Variable	Source
6b	Geopotential Height	ERA5	https://www.ecmwf.int/en/forecasts/dataset/ecmwf-reanalysis-v5
6b	Modes of Variability	Marshall Southern Annular Mode Index	http://www.nerc-bas.ac.uk/icd/gjma/sam.html
6b	Pressure, Sea Level or Near-Surface	ERA5	https://www.ecmwf.int/en/forecasts/dataset/ecmwf-reanalysis-v5
6b	Pressure, Sea Level or Near-Surface	University of Wisconsin-Madison Automated Weather Stations— Antarctic Meteorological Research and Data Center	https://amrdcdata.ssec.wisc.edu
6b	Pressure, Sea Level or Near-Surface	Staffed Weather Station Data	https://legacy.bas.ac.uk/met/READER/
6b	Temperature, [Near] Surface	ERA5	https://www.ecmwf.int/en/forecasts/dataset/ecmwf-reanalysis-v5
6b	Temperature, [Near] Surface	University of Wisconsin-Madison Automated Weather Stations— Antarctic Meteorological Research and Data Center	https://amrdcdata.ssec.wisc.edu
6b	Temperature, [Near] Surface	Staffed Weather Station Data	https://legacy.bas.ac.uk/met/READER/
6b	Temperature, Upper-Atmosphere	ERA5	https://www.ecmwf.int/en/forecasts/dataset/ecmwf-reanalysis-v5
6b	Wind, Upper-Atmosphere	ERA5	https://www.ecmwf.int/en/forecasts/dataset/ecmwf-reanalysis-v5

Section 6c Ice sheet surface mass balance

Sub-section	General Variable or Phenomenon	Specific Dataset or Variable	Source
6c	Atmospheric River	MERRA-2	http://gmao.gsfc.nasa.gov/reanalysis/MERRA-2/
6c	Geopotential Height	ERA5	https://www.ecmwf.int/en/forecasts/dataset/ecmwf-reanalysis-v5
6c	Grounded and Floating Ice Masks	Antarctic Digital Database	https://www.bas.ac.uk/project/add/
6c	Ice Sheet Surface Mass Balance	ERA5	https://www.ecmwf.int/en/forecasts/dataset/ecmwf-reanalysis-v5

Sub-section	General Variable or Phenomenon	Specific Dataset or Variable	Source
6c	Ice Sheet Surface Mass Balance	MERRA-2	http://gmao.gsfc.nasa.gov/reanalysis/MERRA-2/
6c	Ice Sheet Surface Mass Balance	Polar-Oriented Regional Climate Model (Model for Surface Mass Balance of the Arctic Ice Sheets [MAR])	https://arcticdata.io/catalog/view/doi%3A10.18739%2FA28G8FJ7F
6c	Ice Surface Height	CESat-2 ATL15	https://nsidc.org/data/atl15/versions/2

Section 6d Ice sheet melt extent and duration

Sub-section	General Variable or Phenomenon	Specific Dataset or Variable	Source
6d	Ice Sheet Surface Melt	Defense Meteorological Satellite Program (DMSP) Special Sensor Microwave Imager/Sounder (SSMIS)	https://nsidc.org/data/nsidc-0001/versions/6
6d	Sea Ice Extent/Area/Concentration	Nimbus-7 Scanning Multichannel Microwave Radiometer (SMMR) Sea Ice Concentration	https://nsidc.org/data/nsidc-0007

Section 6e Ice sheet mass balance

Sub-section	General Variable or Phenomenon	Specific Dataset or Variable	Source
6e	Ice Sheet Mass	Gravity Recovery and Climate Experiment (GRACE)/GRACE Follow-On (GRACE-FO)	https://podaac.jpl.nasa.gov/dataset/TELLUS_GRAC-GRFO_MASCON_CRI_GRID_RL06_V2
6e	Ice Sheet Surface Height	Advanced Topographic Laser Altimeter System (ATLAS) Ice, Cloud and Land Elevation Satellite-2 (ICESat-2)	https://nsidc.org/data/atl06/versions/5
6e	Ice Sheet Surface Height	ICESat-2	https://icesat-2.gsfc.nasa.gov/

Section 6f Sea ice extent, concentration, and seasonality			
Sub-section	**General Variable or Phenomenon**	**Specific Dataset or Variable**	**Source**
6f	Sea Ice Extent and Area	NIMBUS-7 SMMR and DMSP SSM/I-SSMIS Version 4 (NSIDC-0079)	https://doi.org/10.5067/X5LG68MH013O
6f	Sea Ice Extent and Area	AMSR2 Daily Polar Gridded Sea Ice Concentrations, Version 2 (NSIDC-0803)	https://doi.org/10.5067/W13AO54SS7CW
6f	Sea Ice Extent and Area	Sea Ice Concentration from Nimbus-7 SMMR and DMSP SSM/1-SSMIS Passive Microwave Data, Version 2 (NSIDC-0051)	https://doi.org/10.5067/MPYG15WAA4WX
6f	Sea Surface Temperature	NOAA OISSTv2.1	https://www.ncei.noaa.gov/products/optimum-interpolation-sst

Section 6g Southern Ocean			
Sub-section	**General Variable or Phenomenon**	**Specific Dataset or Variable**	**Source**
6g1	Mixed-Layer Depth	Argo Monthly Climatology	https://sio-argo.ucsd.edu/RG_Climatology.html
6g1	Sea Surface Salinity	Argo Monthly Climatology	https://sio-argo.ucsd.edu/RG_Climatology.html
6g1	Sea Surface Temperature	NOAA OISSTv2.1	https://www.ncei.noaa.gov/products/optimum-interpolation-sst
6g2	Surface Heat flux	ERA5	https://www.ecmwf.int/en/forecasts/dataset/ecmwf-reanalysis-v5
6g3	Ocean Heat Content	Argo Monthly Climatology	https://sio-argo.ucsd.edu/RG_Climatology.html
6g4	Dissolved Oxygen	Biogeochemical Argo (BGC-Argo)	https://biogeochemical-argo.org/
6g4	Ocean Chlorophyll	ESA Ocean Colour Climate Change Initiative (OC-CCI) product Version 6.0	https://www.oceancolour.org/

Section 6h 2024 Antarctic ozone hole			
Sub-section	**General Variable or Phenomenon**	**Specific Dataset or Variable**	**Source**
6h	Ozone, Lower Stratosphere	Ozone, Lower Stratosphere	https://ozonewatch.gsfc.nasa.gov/
6h	Ozone, Lower Stratosphere	Ozonesonde	https://gml.noaa.gov/dv/spo_oz/

Sub-section	General Variable or Phenomenon	Specific Dataset or Variable	Source
6h	Ozone, Total Column and Stratospheric	Ozone Mapping Instrument (OMI) Ozone Mapping & Profiler Suite (OMPS), Total Ozone Mapping Spectrum (TOMS), Earth Probe TOMS	https://ozoneaq.gsfc.nasa.gov/data/ozone/
6h	Temperature, Upper-Atmosphere	MERRA-2	https://gmao.gsfc.nasa.gov/reanalysis/MERRA-2/

Sidebar 6.1: The Exceptional Nature of Supraglacial Meltwater in 2024/25

Sub-section	General Variable or Phenomenon	Specific Dataset or Variable	Source
SB6.1	Modes of Variability	Marshall Southern Annular Mode (SAM) Index (Station-based)	https://climatedataguide.ucar.edu/climate-data/marshall-southern-annular-mode-sam-index-station-based
SB6.1	Surface Meltwater	LandSat 8/9 (L8, L9)	https://www.usgs.gov/landsat-missions/landsat-levels-processing
SB6.1	Temperature, [Near] Surface	ERA5	https://www.ecmwf.int/en/forecasts/dataset/ecmwf-reanalysis-v5

References

Adusumilli, S., and H. A. Fricker, 2025: Ice sheet mass balance [in "State of the Climate in 2024"]. *Bull. Amer. Meteor. Soc.*, **106** (8), S372–S374, https://doi.org/10.1175/BAMS-D-25-0087.1

——, ——, B. Medley, L. Padman, and M. R. Siegfried, 2020: Interannual variations in meltwater input to the Southern Ocean from Antarctic ice shelves. *Nat. Geosci.*, **13**, 616–620, https://doi.org/10.1038/s41561-020-0616-z.

——, ——, and A. S. Gardner, 2022: Ice sheet mass balance [in "State of the Climate in 2021"]. *Bull. Amer. Meteor. Soc.*, **103** (8), S325–S329, https://doi.org/10.1175/BAMS-D-21-0078.1.

Agosta, C., and Coauthors, 2019: Estimation of the Antarctic surface mass balance using the regional climate model MAR (1979–2015) and identification of dominant processes. *Cryosphere*, **13**, 281–296, https://doi.org/10.5194/tc-13-281-2019.

AMRDC, 2022: Antarctic Meteorological Research and Data Center: Automatic weather station quality-controlled observational data. AMRDC Data Repository, accessed 15 January 2025, https://doi.org/10.48567/1hn2-nw60.

Arthur, J. F., C. R. Stokes, S. S. R. Jamieson, J. Rachel Carr, A. A. Leeson, and V. Verjans, 2022: Large interannual variability in supraglacial lakes around East Antarctica. *Nat. Commun.*, **13**, 1711, https://doi.org/10.1038/s41467-022-29385-3.

Baiman, R., A. C. Winters, B. Pohl, V. Favier, J. D. Wille, and K. R. Clem, 2024: Synoptic and planetary-scale dynamics modulate Antarctic atmospheric river precipitation intensity. *Commun. Earth Environ.*, **5**, 127, https://doi.org/10.1038/s43247-024-01307-9.

Banwell, A. F., D. R. MacAyeal, and O. V. Sergienko, 2013: Breakup of the Larsen B ice shelf triggered by chain reaction drainage of supraglacial lakes. *Geophys. Res. Lett.*, **40**, 5872–5876, https://doi.org/10.1002/2013GL057694.

——, I. C. Willis, G. J. Macdonald, B. Goodsell, and D. R. MacAyeal, 2019: Direct measurements of ice-shelf flexure caused by surface meltwater ponding and drainage. *Nat. Commun.*, **10**, 730, https://doi.org/10.1038/s41467-019-08522-5.

——, R. T. Datta, R. L. Dell, M. Moussavi, L. Brucker, G. Picard, C. A. Shuman, and L. A. Stevens, 2021: The 32-year record-high surface melt in 2019/2020 on the northern George VI Ice Shelf, Antarctic Peninsula. *Cryosphere*, **15**, 909–925, https://doi.org/10.5194/tc-15-909-2021.

——, N. Wever, D. Dunmire, and G. Picard, 2023: Quantifying Antarctic-wide ice-shelf surface melt volume using microwave and firn model data: 1980 to 2021. *Geophys. Res. Lett.*, **50**, e2023GL102744, https://doi.org/10.1029/2023GL102744.

Barthélemy, L., F. Codron, J. Wille, V. Favier, and K. R. Clem, 2026: Future atmospheric rivers in Antarctica: Characteristics and impacts with the IPSL model. *J. Geophys. Res. Atmos.*, **131**, e2025JD043398, https://doi.org/10.1029/2025JD043398.

Beadling, R. L., N. M. Freeman, G. A. MacGilchrist, M. Mazloff, J.-R. Shi, A. F. Thompson, and E. Wilson, 2022: Southern Ocean [in "State of the Climate in 2021"]. *Bull. Amer. Meteor. Soc.*, **103** (8), S329–S332, https://doi.org/10.1175/BAMS-D-22-0078.1.

Bell, R. E., and Coauthors, 2017: Antarctic ice shelf potentially stabilized by export of meltwater in surface river. *Nature*, **544**, 344–348, https://doi.org/10.1038/nature22048.

——, A. F. Banwell, L. D. Trusel, and J. Kingslake, 2018: Antarctic surface hydrology and impacts on ice-sheet mass balance. *Nat. Climate Change*, **8**, 1044–1052, https://doi.org/10.1038/s41558-018-0326-3.

Bromwich, D. H., A. Ensign, S.-H. Wang, and X. Zou, 2024: Major artifacts in ERA5 2-m air temperature trends over Antarctica prior to and during the modern satellite era. *Geophys. Res. Lett.*, **51**, e2024GL111907, https://doi.org/10.1029/2024GL111907.

Cheng, L., and Coauthors, 2022: Past and future ocean warming. *Nat. Rev. Earth Environ.*, **3**, 776–794, https://doi.org/10.1038/s43017-022-00345-1.

Clem, K. R., and M. N. Raphael, Eds., 2024: Antarctica and the Southern Ocean [in "State of the Climate in 2023"]. *Bull. Amer. Meteor. Soc.*, **103** (8), S307–S340, https://doi.org/10.1175/BAMS-D-24-0099.1.

Comiso, J. C., 2023: Bootstrap Sea Ice Concentrations from Nimbus-7 SMMR and DMSP SSM/I-SSMIS, Version 4 (NSIDC-0079), NASA National Snow and Ice Data Center Distributed Active Archive Center, Boulder, Colorado USA, accessed 8 October 2025, https://doi.org/10.5067/X5LG68MH013O.

Corr, D., A. Leeson, M. McMillan, C. Zhang, and T. Barnes, 2022: An inventory of supraglacial lakes and channels across the west Antarctic ice sheet. *Earth Syst. Sci. Data*, **14**, 209–228, https://doi.org/10.5194/essd-14-209-2022.

Davison, B. J., and Coauthors, 2023: Sea level rise from West Antarctic mass loss significantly modified by large snowfall anomalies. *Nat. Commun.*, **14**, 1479, https://doi.org/10.1038/s41467-023-36990-3.

de Boyer Montégut, C., G. Madec, A. S. Fischer, A. Lazar, and D. Ludicone, 2004: Mixed layer depth over the global ocean: An examination of profile data and a profile?based climatology. *J. Geophys. Res.*, **109**, C12003, https://doi.org/10.1029/2004JC002378.

Dell, R., N. Arnold, I. Willis, A. Banwell, A. Williamson, H. Pritchard, and A. Orr, 2020: Lateral meltwater transfer across an Antarctic ice shelf. *Cryosphere*, **14**, 2313–2330, https://doi.org/10.5194/tc-14-2313-2020.

Dell, R. L., A. F. Banwell, I. C. Willis, N. S. Arnold, A. R. W. Halberstadt, T. R. Chudley, and H. D. Pritchard, 2022: Supervised classification of slush and ponded water on Antarctic ice shelves using Landsat 8 imagery. *J. Glaciol.*, **68**, 401–414, https://doi.org/10.1017/jog.2021.114.

——, I. C. Willis, N. S. Arnold, A. F. Banwell, and S. De Roda Husman, 2024: Substantial contribution of slush to meltwater area across Antarctic ice shelves. *Nat. Geosci.*, **17**, 624–630, https://doi.org/10.1038/s41561-024-01466-6.

——, M. L. Maclennan, L. Trusel, and M. Bahrami, 2026: Brief communication: Lateral surface meltwater export from Bach Ice Shelf resumes after 9-year hiatus. *EGUsphere*, **2026**, 1–11, https://doi.org/10.5194/egusphere-2026-233.

DiGirolamo, N., C. L., Parkinson, D. J. Cavalieri, P. Gloersen, and H. J. Zwally, 2022: Sea Ice Concentration from Nimbus-7 SMMR and DMSP SSM/I-SSMIS Passive Microwave Data, Version 2 (NSIDC-0051), NASA National Snow and Ice Data Center Distributed Active Archive Center, Boulder, Colorado USA, accessed 19 February 2026, https://doi.org/10.5067/MPYG15WAA4WX.

Doddridge, E. W., and Coauthors, 2025: Impacts of Antarctic summer sea-ice extremes. *PNAS Nexus*, **4**, pgaf164, https://doi.org/10.1093/pnasnexus/pgaf164.

Dunmire, D., N. Wever, A. F. Banwell, and J. T. M. Lenaerts, 2024: Antarctic-wide ice-shelf firn emulation reveals robust future firn air depletion signal for the Antarctic Peninsula. *Commun. Earth Environ.*, **5**, 100, https://doi.org/10.1038/s43247-024-01255-4.

Eayrs, C., X. Li, M. N. Raphael, and D. M. Holland, 2021: Rapid decline in Antarctic sea ice in recent years hints at future change. *Nat. Geosci.*, **14**, 460–464, https://doi.org/10.1038/s41561-021-00768-3.

Foppert, A., K. A. Donohue, D. R. Watts, and K. L. Tracey, 2017: Eddy heat flux across the Antarctic Circumpolar Current estimated from sea surface height standard deviation. *J. Geophys. Res. Oceans*, **122**, 6947–6964, https://doi.org/10.1002/2017JC012837.

Fricker, H. A., B. K. Galton-Fenzi, C. C. Walker, B. I. D. Freer, L. Padman, and R. DeConto, 2025: Antarctica in 2025: Drivers of deep uncertainty in projected ice loss. *Science*, **387**, 601–609, https://doi.org/10.1126/science.adt9619.

Frölicher, T. L., J. L. Sarmiento, D. J. Paynter, J. P. Dunner, J. P. Krasting, and M. Winton, 2015: Dominance of the Southern Ocean in anthropogenic carbon and heat uptake in CMIP5 models. *J. Climate*, **28**, 862–886, https://doi.org/10.1175/JCLI-D-14-00117.1.

Gelaro, R., and Coauthors, 2017: The Modern-Era Retrospective Analysis for Research and Applications, version 2 (MERRA-2). *J. Climate*, **30**, 5419–5454, https://doi.org/10.1175/JCLI-D-16-0758.1.

Gerrish, L., L. Ireland, P. Fretwell, and P. Cooper, 2023: Medium resolution vector polygons of the Antarctic coastline - Version 7.8. NERC EDS UK Polar Data Centre, accessed 18 February 2026, https://doi.org/10.5285/3EA85903-E068-4242-A63F-46767E16F85C.

Gloersen, P., 2006: Nimbus-7 SMMR polar gridded radiances and sea ice concentrations, version 1. Subset used: 37 & 19 GHz, h-polarization, 25 km grid, October 1979–April 1987. NASA National Snow and Ice Data Center Distributed Active Archive Center, accessed 5 May 2020, https://doi.org/10.5067/QOZIVYV3V9JP.

Gudmundsson, G. H., F. S. Paolo, S. Adusumilli, and H. A. Fricker, 2019: Instantaneous Antarctic ice sheet mass loss driven by thinning ice shelves. *Geophys. Res. Lett.*, **46**, 13 903–13 909, https://doi.org/10.1029/2019GL085027.

Hersbach, H., and Coauthors, 2020: The ERA5 global reanalysis. *Quart. J. Roy. Meteor. Soc.*, **146**, 1999–2049, https://doi.org/10.1002/qj.3803.

Himmich, K., M. Vancoppenolle, S. Stammerjohn, M. Bocquet, G. Madec, J.-B. Sallée, and S. Fleury, 2024: Thermodynamics drive post?2016 changes in the Antarctic sea ice seasonal cycle. *J. Geophys. Res. Oceans*, **129**, e2024JC021112, https://doi.org/10.1029/2024JC021112.

Hobbs, W. R., R. Holmes, and A. E. Kiss, 2026: Ocean constraints on winter Antarctic sea ice extent. *J. Geophys. Res. Oceans*, **131**, e2025JC022716, https://doi.org/10.1029/2025JC022716.

Hosking, J. S., A. Orr, G. J. Marshall, J. Turner, and T. Phillips, 2013: The influence of the Amundsen–Bellingshausen Seas Low on the climate of West Antarctica and its representation in coupled climate model simulations. *J. Climate*, **26**, 6633–6648, https://doi.org/10.1175/JCLI-D-12-00813.1.

Huang, B., C. Liu, V. Banzon, E. Freeman, G. Graham, B. Hankins, T. Smith, and H.-M. Zhang, 2021: Improvements of the Daily Optimum Interpolation Sea Surface Temperature (DOISST) version 2.1. *J. Climate*, **34**, 2923–2939, https://doi.org/10.1175/JCLI-D-20-0166.1.

Izeboud, M., B. Wouters, S. De Roda Husman, and S. Lhermitte, 2025: Damage development on Antarctic ice shelves sensitive to climate warming. *Nat. Climate Change*, **15**, 1333–1339, https://doi.org/10.1038/s41558-025-02453-4.

Josey, S. A., J. P. Grist, J. V. Mecking, B. I. Moat, and E. Schulz, 2023: A clearer view of Southern Ocean air-sea interaction using surface heat flux asymmetry. *Philos. Trans. Roy. Soc.*, **A381**, 20220067, https://doi.org/10.1098/rsta.2022.0067.

——, A. J. S. Meijers, A. T. Blaker, J. P. Grist, J. Mecking, and H. C. Ayres, 2024: Record-low Antarctic sea ice in 2023 increased ocean heat loss and storms. *Nature*, **636**, 635–639, https://doi.org/10.1038/s41586-024-08368-y.

Kimura, N., and M. Wakatsuchi, 2011: Large-scale processes governing the seasonal variability of the Antarctic sea ice. *Tellus*, **63A**, 828–840, https://doi.org/10.1111/j.1600-0870.2011.00526.x.

Kingslake, J., J. C. Ely, I. Das, and R. E. Bell, 2017: Widespread movement of meltwater onto and across Antarctic ice shelves. *Nature*, **544**, 349–352, https://doi.org/10.1038/nature22049.

Kittel, C., and Coauthors, 2021: Diverging future surface mass balance between the Antarctic ice shelves and grounded ice sheet. *Cryosphere*, **15**, 1215–1236, https://doi.org/10.5194/tc-15-1215-2021.

Kuipers Munneke, P., S. R. M. Ligtenberg, M. R. Van Den Broeke, and D. G. Vaughan, 2014: Firn air depletion as a precursor of Antarctic ice-shelf collapse. *J. Glaciol.*, **60**, 205–214, https://doi.org/10.3189/2014JoG13J183.

Lait, L. R., P. A. Newman, N. A. Kramarova, B. Johnson, M. L. Santee, I. Petropavlovskikh, L. Coy, and J. De Laat, 2025: 2024 Antarctic ozone hole [in "State of the Climate in 2024"]. *Bull. Amer. Meteor. Soc.*, **106** (8), S388–S390, https://doi.org/10.1175/BAMS-D-25-0087.1.

Leeson, A. A., E. Forster, A. Rice, N. Gourmelen, and J. M. Van Wessem, 2020: Evolution of supraglacial lakes on the Larsen B ice shelf in the decades before it collapsed. *Geophys. Res. Lett.*, **47**, e2019GL085591, https://doi.org/10.1029/2019GL085591.

MacFerrin, M., T. Mote, H. Wang, L. Liu, L. Montgomery, and T. Scambos, 2021: Ice sheet seasonal melt extent and duration [in "State of the Climate in 2020"]. *Bull. Amer. Meteor. Soc.*, **102** (8), S331–S334, https://doi.org/10.1175/BAMS-D-21-0081.1.

——, ——, A. F. Banwell, and T. Scambos, 2025: Ice sheet seasonal melt extent and duration [in "State of the Climate in 2024"]. *Bull. Amer. Meteor. Soc.*, **106** (8), S372–S374, https://doi.org/10.1175/BAMS-D-25-0087.1.

Maclennan, M. L., and Coauthors, 2023: Climatology and surface impacts of atmospheric rivers on West Antarctica. *Cryosphere*, **17**, 865–881, https://doi.org/10.5194/tc-17-865-2023.

Mahagaonkar, A., G. Moholdt, Q. Glaude, and T. V. Schuler, 2024: Supraglacial lake evolution and its drivers in Dronning Maud Land, East Antarctica. *J. Glaciol.*, **70**, e49, https://doi.org/10.1017/jog.2024.66.

Maksym, T., and S. Stammerjohn, 2026: The rise and fall of Antarctic sea ice: Large-scale variability. Sea Ice: Its Physics, Chemistry, Biology, Geology and Societal Importance, D. N. Thomas, Ed., Wiley, 215–260, https://doi.org/10.1002/9781394213764.ch06.

Manney, G. L., and Coauthors, 2011: Unprecedented Arctic ozone loss in 2011. *Nature*, **478**, 469–475, https://doi.org/10.1038/nature10556.

Marshall, G. J., 2003: Trends in the Southern Annular Mode from observations and reanalyses. *J. Climate*, **16**, 4134–4143, https://doi.org/10.1175/1520-0442(2003)016<4134:TITSAM>2.0.CO;2.

Massom, R. A., T. A. Scambos, L. G. Bennetts, P. Reid, V. A. Squire, and S. E. Stammerjohn, 2018: Antarctic Ice Shelf disintegration triggered by sea ice loss and ocean swell. *Nature*, **558**, 383–389, https://doi.org/10.1038/s41586-018-0212-1.

Medley, B., and E. R. Thomas, 2019: Increased snowfall over the Antarctic ice sheet mitigated twentieth-century sea-level rise. *Nat. Climate Change*, **9**, 34–39, https://doi.org/10.1038/s41558-018-0356-x.

Meier, W. N., H. Wilcox, M. A. Hardman, and J. S. Stewart, 2019: DMSP SSM/I-SSMIS daily polar gridded brightness temperatures, version 5. Subset used: 37 & 19 GHz, h-polarization, 25 km grid, October 1987–April 2020. NASA National Snow and Ice Data Center Distributed Active Archive Center, accessed 11 February 2021, https://doi.org/10.5067/QU2UYQ6T0B3P.

Meredith, M. P., and M. A. Brandon, 2017: Oceanography and sea ice in the Southern Ocean. *Sea Ice*, D. Thomas, Ed., Wiley, 216–238.

Millán, L., and Coauthors, 2024: The evolution of the Hunga hydration in a moistening stratosphere. *Geophys. Res. Lett.*, **51**, e2024GL110841, https://doi.org/10.1029/2024GL110841.

Mote, T. L., 2007: Greenland surface melt trends 1973–2007: Evidence of a large increase in 2007. *Geophys. Res. Lett.*, **34**, L22507, https://doi.org/10.1029/2007GL031976.

——, and M. R. Anderson, 1995: Variations in snowpack melt on the Greenland ice sheet based on passive-microwave measurements. *J. Glaciol.*, **41**, 51–60, https://doi.org/10.3189/S0022143000017755.

Mottram, R., and Coauthors, 2021: What is the surface mass balance of Antarctica? *An intercomparison of regional climate model estimates. Cryosphere*, **15**, 3751–3784, https://doi.org/10.5194/tc-15-3751-2021.

Moussavi, M., A. Pope, A. Halberstadt, L. Trusel, L. Cioffi, and W. Abdalati, 2020: Antarctic supraglacial lake detection using Landsat 8 and Sentinel-2 imagery: Towards continental generation of lake volumes. *Remote Sens.*, **12**, 134, https://doi.org/10.3390/rs12010134.

Newman, P. A., E. R. Nash, S. R. Kawa, S. A. Montzka, and S. M. Schauffler, 2006: When will the Antarctic ozone hole recover? *Geophys. Res. Lett.*, **33**, L12814, https://doi.org/10.1029/2005GL025232.

Norwegian Polar Institute, 2018: Quantarctica v3.0, detailed basemap. https://www.npolar.no/quantarctica/.

Ochwat, N. E., and Coauthors, 2024: Triggers of the 2022 Larsen B multi-year landfast sea ice breakout and initial glacier response. *Cryosphere*, **18**, 1709–1731, https://doi.org/10.5194/tc-18-1709-2024.

Orr, A., G. J. Marshall, J. C. R. Hunt, J. Sommeria, C.-G. Wang, N. P. M. van Lipzig, D. Cresswell, and J. C. King, 2008: Characteristics of summer airflow over the Antarctic Peninsula in response to recent strengthening of westerly circumpolar winds. *J. Atmos. Sci.*, **65**, 1396–1413, https://doi.org/10.1175/2007JAS2498.1.

Orsi, A. H., T. Whitworth III, and W. D. Nowlin Jr., 1995: On the meridional extent and fronts of the Antarctic Circumpolar Current. *Deep-Sea. Res. I*, **42**, 641–673, https://doi.org/10.1016/0967-0637(95)00021-W.

Otosaka, I. N., and Coauthors, 2023: Mass balance of the Greenland and Antarctic ice sheets from 1992 to 2020. *Earth Syst. Sci. Data*, **15**, 1597–1616, https://doi.org/10.5194/essd-15-1597-2023.

Pellichero, V., J.-B. Sallée, S. Schmidtko, F. Roquet, and J.-B. Charrassin, 2017: The ocean mixed layer under Southern Ocean sea-ice: Seasonal cycle and forcing. *J. Geophys. Res. Oceans*, **122**, 1608–1633, https://doi.org/10.1002/2016JC011970.

Pezzi, L. P., and Coauthors, 2023: Southern Ocean [in "State of the Climate in 2022"]. *Bull. Amer. Meteor. Soc.*, **104** (9), S351–S355, https://doi.org/10.1175/BAMS-D-23-0077.1.

Purich, A., and E. W. Doddridge, 2023: Record low Antarctic sea ice coverage indicates a new sea ice state. *Commun. Earth Environ.*, **4**, 314, https://doi.org/10.1038/s43247-023-00961-9.

Raphael, M. N., and K. R. Clem, Eds., 2025: Antarctica and the Southern Ocean [in "State of the Climate in 2024"]. *Bull. Amer. Meteor. Soc.*, **106** (8), S357–S400, https://doi.org/10.1175/BAMS-D-25-0087.1.

Reid, P., S. Stammerjohn, R. A. Massom, S. Barreira, T. Scambos, and J. L. Lieser, 2024: Sea ice extent, concentration, and seasonality [in "State of the Climate in 2023"]. *Bull. Amer. Meteor. Soc.*, **105** (8), S351–S354, https://doi.org/10.1175/BAMS-D-24-0099.1.

——, ——, ——, ——, ——, and ——, 2025: Sea ice extent, concentration, and seasonality [in "State of the Climate in 2024"]. *Bull. Amer. Meteor. Soc.*, **106** (8), S378–S381, https://doi.org/10.1175/2025BAMSStateoftheClimate.1.

Reid, P. A., and R. A. Massom, 2022: Change and variability in Antarctic coastal exposure, 1979-2020. *Nat. Commun.*, **13**, 1164, https://doi.org/10.1038/s41467-022-28676-z.

Reynolds, R. W., N. A. Rayner, T. M. Smith, D. C. Stokes, and W. Wang, 2002: An improved in situ and satellite SST analysis for climate. *J. Climate*, **15**, 1609–1625, https://doi.org/10.1175/1520-0442(2002)015<1609:AIISAS>2.0.CO;2.

Riihelä, A., R. M. Bright, and K. Anttila, 2021: Recent strengthening of snow and ice albedo feedback driven by Antarctic sea-ice loss. *Nat. Geosci.*, **14**, 832–836, https://doi.org/10.1038/s41561-021-00841-x.

Roemmich, D., and J. Gilson, 2009: The 2004–2008 mean and annual cycle of temperature, salinity, and steric height in the global ocean from the Argo Program. *Prog. Oceanogr.*, **82**, 81–100, https://doi.org/10.1016/j.pocean.2009.03.004.

Santee, M. L., and Coauthors, 2024: The influence of stratospheric hydration from the Hunga eruption on chemical processing in the 2023 Antarctic vortex. ESS Open Archive, accessed 16 January 2024, https://doi.org/10.22541/essoar.170542085.55151307/v1.

Sathyendranath, S., and Coauthors, 2019: An ocean-colour time series for use in climate studies: The experience of the Ocean-Colour Climate Change Initiative (OC-CCI). *Sensors*, **19**, 4285, https://doi.org/10.3390/s19194285.

Scambos, T. A., C. Hulbe, M. Fahnestock, and J. Bohlander, 2000: The link between climate warming and break-up of ice shelves in the Antarctic Peninsula. *J. Glaciol.*, **46**, 516–530, https://doi.org/10.3189/172756500781833043.

——, E. Berthier, T. Haran, C. A. Shuman, A. J. Cook, S. R. M. Ligtenberg, and J. Bohlander, 2014: Detailed ice loss pattern in the northern Antarctic Peninsula: Widespread decline driven by ice front retreats. *Cryosphere*, **8**, 2135–2145, https://doi.org/10.5194/tc-8-2135-2014.

Silvano, A., and Coauthors, 2025: Rising surface salinity and declining sea ice: A new Southern Ocean state revealed by satellites. *Proc. Natl. Acad. Sci. USA*, **122**, e2500440122, https://doi.org/10.1073/pnas.2500440122.

Smith, B., and Coauthors, 2020: Pervasive ice sheet mass loss reflects competing ocean and atmosphere processes. *Science*, **368**, 1239–1242, https://doi.org/10.1126/science.aaz5845.

——, B. P. Jelley, S. Dickinson, T. Sutterley, T. Neumann, and K. Harbeck, 2024: ATLAS/ICESat-2 L3B gridded Antarctic and Greenland height change, version 4. NASA National Snow and Ice Data Center Distributed Active Archive Center, accessed 16 February 2026, https://doi.org/10.5067/ATLAS/ATL15.004.

Spira, T., S. Swart, I. Giddy, and M. Du Plessis, 2024: The observed spatiotemporal variability of Antarctic winter water. *J. Geophys. Res. Oceans*, **129**, e2024JC021017, https://doi.org/10.1029/2024JC021017.

Stammerjohn, S. E., D. G. Martinson, R. C. Smith, X. Yuan, and D. Rind, 2008: Trends in Antarctic annual sea ice retreat and advance and their relation to El Niño–Southern Oscillation and Southern Annular Mode variability. *J. Geophys. Res.*, **113**, C03S90, https://doi.org/10.1029/2007JC004269.

Stewart, J. S., W. N. Meier, R. Marowitz, D. J. Scott, and H. Wilcox, 2025: AMSR2 Daily Polar Gridded Sea Ice Concentrations, Version 2 (NSIDC-0803), NASA National Snow and Ice Data Center Distributed Active Archive Center, Boulder, Colorado USA, accessed 19 February 2026, https://doi.org/10.5067/W13AO54SS7CW.

Stokes, C. R., J. E. Sanderson, B. W. J. Miles, S. S. R. Jamieson, and A. A. Leeson, 2019: Widespread distribution of supraglacial lakes around the margin of the East Antarctic ice sheet. *Sci. Rep.*, **9**, 13823, https://doi.org/10.1038/s41598-019-50343-5.

The Firn Symposium Team, 2024: Firn on ice sheets. *Nat. Rev. Earth Environ.*, **5**, 79–99, https://doi.org/10.1038/s43017-023-00507-9.

The IMBIE Team, 2020: Mass balance of the Greenland ice sheet from 1992 to 2018. *Nature*, **579**, 233–239, https://doi.org/10.1038/s41586-019-1855-2.

Thomalla, S., and Coauthors, 2024: Southern Ocean [in "State of the Climate in 2023"]. *Bull. Amer. Meteor. Soc.*, **105** (8), S355–S356, https://doi.org/10.1175/BAMS-D-24-0099.1.

——, and Coauthors, 2025: Southern Ocean [in "State of the Climate in 2024"]. *Bull. Amer. Meteor. Soc.*, **106** (8), S384–S387, https://doi.org/10.1175/BAMS-D-25-0087.1.

Thomas, D., Ed., 2017: Sea Ice. 3rd ed. Wiley-Blackwell, 664 pp.

Trusel, L. D., K. E. Frey, S. B. Das, K. B. Karnauskas, P. Kuipers Munneke, E. Van Meijgaard, and M. R. Van Den Broeke, 2015: Divergent trajectories of Antarctic surface melt under two twenty-first-century climate scenarios. *Nat. Geosci.*, **8**, 927–932, https://doi.org/10.1038/ngeo2563.

——, Z. Pan, and M. Moussavi, 2022: Repeated tidally induced hydrofracture of a supraglacial lake at the Amery Ice Shelf grounding zone. *Geophys. Res. Lett.*, **49**, e2021GL095661, https://doi.org/10.1029/2021GL095661.

Tuckett, P. A., A. J. Sole, S. J. Livingstone, J. M. Jones, J. M. Lea, and E. Gilbert, 2025: Continent-wide mapping shows increasing sensitivity of East Antarctica to meltwater ponding. *Nat. Climate Change*, **15**, 775–783, https://doi.org/10.1038/s41558-025-02363-5.

Turner, J., and Coauthors, 2004: The SCAR READER project: Toward a high-quality database of mean Antarctic meteorological observations. *J. Climate*, **17**, 2890–2898, https://doi.org/10.1175/1520-0442(2004)017<2890:TSRPTA>2.0.CO;2.

van Wessem, J. M., and Coauthors, 2018: Modelling the climate and surface mass balance of polar ice sheets using RACMO2 – Part II: Antarctica (1979–2016). *Cryosphere*, **12**, 1479–1498, https://doi.org/10.5194/tc-12-1479-2018.

Veldhuijsen, S. B. M., W. J. Van De Berg, P. Kuipers Munneke, and M. R. Van Den Broeke, 2024: Firn air content changes on Antarctic ice shelves under three future warming scenarios. *Cryosphere*, **18**, 1983–1999, https://doi.org/10.5194/tc-18-1983-2024.

Wiese, D. N., D,-N. Yuan, C. Boening, F. W. Landerer, and M. M. Watkins, 2023a: JPL GRACE Mascon Ocean, ice, and hydrology equivalent water height RL06.1 CRI filtered version 03. Ver. RL06.1Mv03. PO.DAAC, accessed 10 February 2026, https://doi.org/10.5067/TEMSC-3JC63.

——, ——, ——, ——, and ——s, 2023b: Tellus level-4 ocean mass anomaly time series from JPL GRACE/GRACE-FO Mascon CRI filtered release 06.1 version 03. Ver. RL06.1Mv03, PO.DAAC, accessed 10 February 2026, https://doi.org/10.5067/TEMSC-AT613.

Wille, J. D., and Coauthors, 2021: Antarctic atmospheric river climatology and precipitation impacts. *J. Geophys. Res. Atmos.*, **126**, e2020JD033788, https://doi.org/10.1029/2020JD033788.

——, and Coauthors, 2025: Atmospheric rivers in Antarctica. *Nat. Rev. Earth Environ.*, **6**, 178–192, https://doi.org/10.1038/s43017-024-00638-7.

Wilson, E. A., L. Arlen, and E. C. Campbell, 2026: Recent extremes in Antarctic sea ice extent modulated by ocean heat ventilation. *Proc. Natl. Acad. Sci. U.S.A.*, **123**, e2530832123, https://doi.org/10.1073/pnas.2530832123.

WMO, 2022: Scientific Assessment of Ozone Depletion: 2022. GAW Rep. 278, 509 pp.

Wong, A. P. S., and Coauthors, 2020: Argo Data 1999–2019: Two Million Temperature-Salinity Profiles and Subsurface Velocity Observations From a Global Array of Profiling Floats. *Front. Mar. Sci.*, **7**, 700, https://doi.org/10.3389/fmars.2020.00700.